The rise and fall of an extraordinary Ca-rich transient

The discovery of ATLAS19dqr/SN 2019bkc[⋆]

S. J. Prentice[1,2,18], K. Maguire[1], A. Flörs[3,4,5], S. Taubenberger[3], C. Inserra[6], C. Frohmaier[7], T. W. Chen[8],
J. P. Anderson[9], C. Ashall[10], P. Clark[2], M. Fraser[11], L. Galbany[12], A. Gal-Yam[13], M. Gromadzki[14], C. P. Gutiérrez[15],
P. A. James[16], P. G. Jonker[17,18], E. Kankare[19], G. Leloudas[20], M. R. Magee[1], P. A. Mazzali[16,3], M. Nicholl[21,22],
M. Pursiainen[15], K. Skillen[1], S. J. Smartt[2], K. W. Smith[2], C. Vogl[3], and D. R. Young[2]

(Affiliations can be found after the references)

ABSTRACT

This work presents the observations and analysis of ATLAS19dqr/SN 2019bkc, an extraordinary rapidly evolving transient event located in an isolated environment, tens of kiloparsecs from any likely host. Its light curves rise to maximum light in $5-6$ d and then display a decline of $\Delta m_{15} \sim 5$ mag. With such a pronounced decay, it has one of the most rapidly evolving light curves known for a stellar explosion. The early spectra show similarities to normal and "ultra-stripped" type Ic SNe, but the early nebular phase spectra, which were reached just over two weeks after explosion, display prominent calcium lines, marking SN 2019bkc as a Ca-rich transient. The Ca emission lines at this phase show an unprecedented and unexplained blueshift of $10\,000-12\,000$ km s^{-1}. Modelling of the light curve and the early spectra suggests that the transient had a low ejecta mass of $0.2-0.4\,M_{\odot}$ and a low kinetic energy of $(2-4) \times 10^{50}$ erg, giving a specific kinetic energy $E_{\rm k}/M_{\rm ej} \sim 1$ [10^{51} erg]/$M_{\odot}$. The origin of this event cannot be unambiguously defined. While the abundance distribution used to model the spectra marginally favours a progenitor of white dwarf origin through the tentative identification of Ar II, the specific kinetic energy, which is defined by the explosion mechanism, is found to be more similar to an ultra-stripped core-collapse events. SN 2019bkc adds to the diverse range of physical properties shown by Ca-rich events.

Key words. supernovae: individual: SN 2019bkc

1. Introduction

The advent of large-scale high-cadence transient surveys in the past decade has led to the discovery of new classes of transients that lie significantly outside the parameter space of traditional classes of supernovae (SNe). In particular, the many repeat visits to the same patch of sky has led to a dramatic increase in the number of transients that are much faster evolving than typically seen in more traditional events, such as SNe Ia, Ibc, II. Some of these are highly luminous and rapidly evolving (Prentice et al. 2018a; Pursiainen et al. 2018; Drout et al. 2014; Poznanski et al. 2010), while others are "faint" and fast evolving events (e.g. Perets et al. 2010; Kasliwal et al. 2010; Drout et al. 2013; Valenti et al. 2014; Inserra et al. 2015). These faint events were missed in shallower, lower cadence surveys and recent results suggest there may be large populations of these events that previously went undetected (e.g. Frohmaier et al. 2018).

The untargeted nature of these recent transient searches compared to previous galaxy-targeted surveys has also resulted in a more complete census of transients occurring in locations that are significantly offset (>10 kpc) from their host galaxy centres. The class of so-called "Ca-rich" transients are of particular interest, they are named after the unusually strong forbidden [Ca II] emission (relative to typical [O I] lines) that develop in their spectra a few months after maximum (for a definition, see Kasliwal et al. 2012). At early times, the spectra of most Ca-rich events show He I features with SN-like velocities of

$\sim 10\,000$ km s^{-1} and they are most commonly classified as peculiar Type Ib SNe from maximum-light spectroscopy (Perets et al. 2010; Gal-Yam 2017). However, their fast evolution to an optically thin regime ("nebular phase") and large [Ca II] to [O I] ratio differentiates them from typical Ib SNe. Although the sample size of Ca-rich events is small because of their faintness and fast evolution, the intrinsic rate of Ca-rich transients is measured to be very high at 33–94% of the local volumetric SN Ia rate (Frohmaier et al. 2018).

The majority of Ca-rich transients occur in an unusual parameter space of galaxy environments; they prefer galaxy group environments with large offsets from early-type galaxies, which suggests an association with an old stellar population (Perets et al. 2010; Lyman et al. 2013, 2016; Lunnan et al. 2017). Strict limits on underlying dwarf galaxies or globular clusters have also been placed (Lyman et al. 2013, 2016). Their preference for offsets from their potential host galaxies can be explained by a very old metal-poor stellar population (Yuan et al. 2013). The observed (and unexplained) Ca enrichment of the intra-cluster medium can be explained with a significant rate of Ca-rich transients (Mulchaey et al. 2014; Frohmaier et al. 2018).

The origin of Ca-rich events is an area under much debate and a number of explosion channels have been suggested. The most obvious explanation given their preference for remote locations in galaxy groups and clusters is a system involving a white dwarf. Proposed models involving a white dwarf include a He-shell detonation on the surface of a white dwarf (Perets et al. 2010; Shen et al. 2010; Woosley & Kasen 2011; Waldman et al. 2011; Sim et al. 2012), the tidal disruption (and detonation) of a white dwarf by an intermediate-mass black

hole (Rosswog et al. 2008; MacLeod et al. 2014; Sell et al. 2015), or the merger of a white dwarf with a neutron star (Metzger 2012; Margalit & Metzger 2016). The white tidal disruption model is expected to produce an X-ray signature (e.g. Sell et al. 2015), which has not been observed in a Ca-rich event as of yet. To explain the large offset and the lack of underlying stellar population, it has been suggested that the objects were not formed at their explosion positions but travelled to these locations perhaps due to a SN kick (Lyman et al. 2014) or interaction with a supermassive black hole (Foley 2015). However, one argument in favour of this "kicked" scenario based on the line shift of the [Ca II] feature (Foley 2015) has been questioned by Milisavljevic et al. (2017) because of the lack of a coeval observed shift in the O I lines. Netherthless, there is still a relative lack of Ca-rich SNe within galaxies which would need to be explained. The need for formation at a different location to explosion is somewhat mitigated by the discovery of the association of these events with group or cluster environments since the intracluster space may contain more stars due to galaxy-galaxy interaction and galaxy mergers than typically found at large distances from galaxies in non-cluster environments. Additionally, SNe Ia can be found in these environments (Gal-Yam et al. 2013).

A minority of events that show Ca-rich spectra at late times have also been detected in star-forming galaxies, such as the unusually slowly evolving and brighter than normal iPTF15eqv that also displayed $H\alpha$ emission in its late-time spectra (Milisavljevic et al. 2017) or with double-peaked light curves (SN 2014ft/iPTF14gqr and iPTF16hgs; De et al. 2018a,b). It is likely that the events associated with higher star-formation environments are not members of the strict class of "Ca-rich" events as defined (see Kasliwal et al. 2012; Lunnan et al. 2017) and their progenitor may be towards the lower end of the core-collapse progenitor mass range ($<12\,M_\odot$, see Suh et al. 2011; Milisavljevic et al. 2017; De et al. 2018b), perhaps ones that are highly stripped in binary systems (Tauris et al. 2015; Moriya et al. 2017).

In this work we present the observations and analysis of the rapidly evolving Ca-rich transient, ATLAS19dqr/SN 2019bkc, which shows, for the first time in a Ca-rich event, a very large shift in its [Ca II] lines of nearly $11\,000\,\mathrm{km\,s^{-1}}$ at ~3 weeks after explosion. An analysis of SN 2019bkc was presented in Chen et al. (2020) in which they noted its rapid light curve and classification as a "peculiar SN I" but lacked the late-time spectra that confirm it to be of the Ca-rich class. Stricter pre-detection photometry limits presented here also place tighter constraints on the evolution of the early-light curve (Sect. 3). In Sect. 2 we discuss the discovery and host-environment, while the photometric and spectroscopic data are presented in Sects. 3 and 4 respectively. In Sect. 5 the photospheric spectra are modelled in order to determine physical characteristics of the explosions. Section 6 covers the discussion of our results and the possible scenarios that may have led to this explosion. finally, in Sect. 7 we bring together our conclusions and summarise the paper.

2. Observations

ATLAS19dqr was discovered by the ATLAS survey (Tonry et al. 2018) on 2019-03-02 10:24:57 UT (MJD 58544.43) at a magnitude of 17.59 in the ATLAS o band (Tonry et al. 2019). It was subsequently reported to the Transient Name Server[1] (TNS) and was given the designation of SN 2019bkc, which we use throughout. There were robust non-detections in the ATLAS

o-band on the four individual 30 s frames taken around the mean time of MJD 58540.45. Forced photometry on each of these provided a flux limit and the weighted mean and standard deviation of these flux measurements was $5.2 \pm 14.4\,\mu\mathrm{Jksy}$. This corresponds to a 3σ upper limit of $o > 19.8$ AB mag. The transient had been observed prior to the ATLAS discovery by the Zwicky Transient Facility (ZTF; Bellm et al. 2019) on 2019-02-27 06:07:40 UT (MJD 58541.26) at $g = 18.9 \pm 0.1$ mag, obtained from the LASAIR broker (Smith et al. 2019).

Multi-colour *ugriz* photometry with the IO:O imager on the Liverpool Telescope (LT; Steele et al. 2004) commenced on 2019-03-03 22:34:54 UT (MJD 58546.02) and was reduced using the standard IO:O pipeline. Aperture photometry was performed on the field using a series of custom PYTHON scripts utilising PYRAF and calibrated to the Sloan Digital Sky Survey photometric system (Ahn et al. 2012).

SN 2019bkc was also observed as part of the GREAT survey (Chen et al. 2018), using the Gamma-Ray Burst Optical/Near-Infrared Detector (GROND; Greiner et al. 2008), a 7-channel imager that collects multi-colour photometry simultaneously in the $g'r'i'z'JHKs$ bands, which is mounted at the 2.2 m MPG telescope at European Southern Observatory (ESO) La Silla Observatory in Chile. The images were reduced by the GROND pipeline (Krühler et al. 2008), which applies de-bias and flat-field corrections, stacks images, and provides astrometric calibration.

Optical spectroscopy of SN 2019bkc using SPRAT (Piascik et al. 2014) on the LT was also obtained starting 1.5 d after discovery and were reduced using the standard SPRAT pipeline (Piascik et al. 2014) with a further flux calibration to a standard star from the Oke (1990) catalogue. Two epochs of optical spectroscopy and one epoch of photometry were obtained with the EFOSC2 imaging spectrograph (Buzzoni et al. 1984) on the ESO New Technology Telescope as part of the extended Public ESO Spectroscopic Survey of Transient Objects (ePESSTO; Smartt et al. 2015). At each epoch both grism #11 (13.8 Å resolution) and grism #16 (13.4 Å resolution) spectra were obtained and were reduced using the custom pipeline described in Smartt et al. (2015).

X-shooter (Vernet et al. 2011) on ESO's Very Large Telescope (VLT) was used to obtain two epochs of optical and near-infrared (NIR) spectroscopy. The spectra were initially reduced using the Reflex software package (Modigliani et al. 2010; Freudling et al. 2013) to produce two-dimensional spectra, which were then extracted using a custom-built pipeline[2]. Spectroscopic observations will be made publicly available on The Weizmann Interactive Supernova Data Repository (WISeREP)[3].

2.1. Swift X-ray observation

We observed the field of SN 2019bkc on MJD 58583.09 with the *Neil Gehrels Swift* Observatory (*Swift*) X-ray telescope (XRT) The XRT data were reduced using the HEASARC FTOOLS pipeline XRTPIPELINE. In a circle with radius of 47″ (this is the 90% encircled energy radius at 1.5 keV) centred on the optical source position, we find two X-ray photons in an effective exposure time of 2767 s. In a source-free circular region on the sky close to the source with a radius of 200″, we found 52 background counts, making the expectation value for the background at the location of SN 2019bkc 2.9 counts. Following Kraft et al. (1991), we derived a 95% confidence level upper limit of 4.5 source counts or $1.6 \times 10^{-3}\,\mathrm{counts\,s^{-1}}$. Using
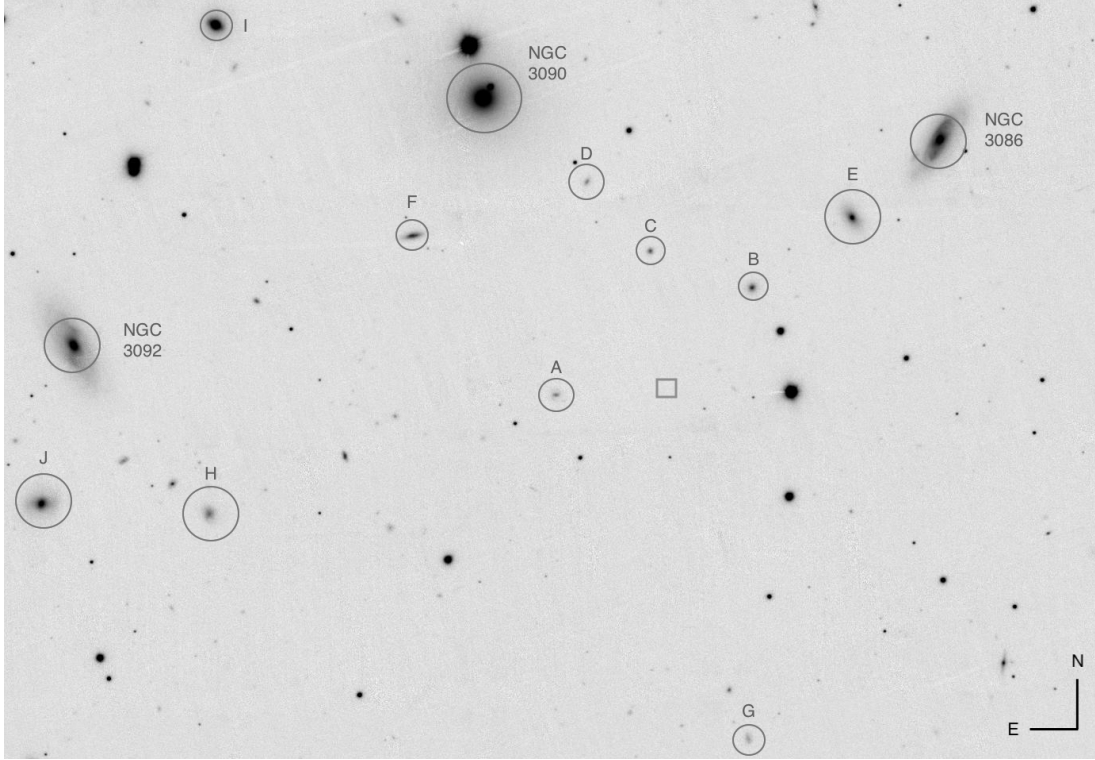

Fig. 1. Stacked archive PanSTARRS g-band image showing galaxies in the region around SN 2019bkc (square). The labelled galaxies are at the redshift of the NGC 3090 galaxy group ($z = 0.020$), apart from two significantly more distant galaxies at $z = 0.188$ (labelled A and C) that are within 100 arcsec of the position of SN 2019bkc.

Table 1. Galaxies with measured redshifts within 400 arcsec of the position of SN 2019bkc.

Galaxy	z	Angular separation [arcsec]	Projected distance [kpc]
A – 2dFGRS TGN216Z080	0.188	69.29	306.7
B – 2dFGRS TGN216Z084	0.019	84.58	34.1
C – 2dFGRS TGN216Z082	0.188	88.19	393.7
D – 2dFGRS TGN216Z079	0.018	140.28	52.0
E – 2dFGRS TGN216Z089	0.022	160.51	74.5
F – 2dFGRS TGN217Z150	0.023	187.02	91.0
NGC 3090	0.020	219.02	94.6
[*]G – 2dFGRS TGN216Z085	0.043	225.02	209.8
NGC 3086	0.023	234.56	113.0
[†]6dFGS gJ100027.0-025650	0.022	270.67	128.9
H – 2dFGRS TGN216Z069	0.023	297.15	145.9
I – 2dFGRS TGN216Z072	0.020	365.04	159.0
[†]2dFGRS TGN216Z103	0.022	365.86	171.2
NGC 3092	0.020	373.83	158.0
J – 2dFGRS TGN217Z145	0.019	399.60	147.7

Notes. The labels (A–J) correspond to those shown on Fig. 1. [†]Outside the field of view of Fig. 1. [*]This is an updated redshift obtained with the LT:SPRAT. The previously reported redshift from Colless et al. (2001) was $z = 0.0003$.

W3PIMMS[4] with $N_H = 5 \times 20$ cm^{-2} and a power law model with an index of 2.0 for the assumed source spectral energy distribution (SED), we converted this limit to an unabsorbed 0.2–10 keV flux of 6.6×10^{-14} erg cm^{-2} s^{-1}, corresponding to a luminosity of $<6.3 \times 10^{40}$ erg s^{-1}.

2.2. Host environment and redshift

SN 2019bkc was observed in a region densely populated by galaxies (Fig. 1, properties tabulated in Table 1), which contains a galaxy group with members in the redshift range of 0.018–0.022. There is no host visible at the position of SN 2019bkc and pre-explosion imaging from the Dark Energy Camera Legacy Survey[5] (DECaLS; Dey et al. 2019) puts a limit of $g \sim 24.7$ mag,

---

[4] https://heasarc.gsfc.nasa.gov/cgi-bin/Tools/w3pimms/w3pimms.pl
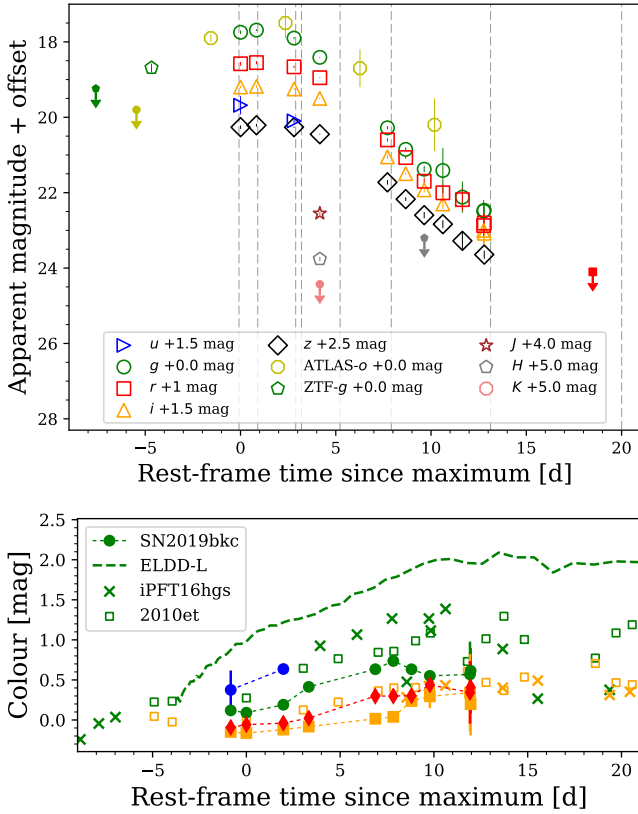
[5] https://datalab.noao.edu/

Fig. 2. *Top*: multi-colour light curves of SN 2019bkc from ZTF, ATLAS, LT, GROND, and NTT. NIR observations are from GROND and the LT. The grey dashed lines denote spectroscopic observations. *Bottom*: colour evolution in $u - g$ (blue), $g - r$ (green), $r - i$ (orange), and $i - z$ (red). The dashed line is the $g - r$ colour curve of the Sim et al. (2012) low-mass edge-lit double detonation (ELDD-L) model and SN 2019bkc is seen to be significantly bluer than this model. Also shown are the $g - r$ and $r - i$ colour curves of iPTF16hgs (De et al. 2018b) and SN 2010et (Kasliwal et al. 2012), with the latter requiring interpolation to match the observed dates.

$r \sim 23.9$ mag, $z \sim 23.0$ mag on any underlying non-detected host. The brightest galaxy in the MKW1 group, NGC 3090, is a giant elliptical galaxy with a redshift of 0.0203 (Morgan et al. 1975; Faber et al. 1989).

Similar to Chen et al. (2020), we assumed that SN 2019bkc is associated with the galaxy group, MKW1 (Morgan et al. 1975), and have adopted a redshift of 0.020 for the transient for two reasons: firstly, this is the redshift of the most massive galaxy in the cluster and therefore the most likely host, and secondly, this is the mean of the redshifts of the galaxies in the cluster. There is a more distant group of galaxies at $z \sim 0.2$ immediately surrounding the transient but exclude any of these as the potential host on the basis that the photospheric-phase spectra are a better match for SNe at $z \sim 0.02$ (see Sect. 4).

Using Nine-year Wilkinson Microwave Anisotropy Probe cosmological parameters $H_0 = 69.32 \, \text{km s}^{-1} \, \text{Mpc}^{-1}$, $\Omega_m = 0.286$, $\Omega_\Lambda = 0.714$ (Hinshaw et al. 2013) and a redshift of $z = 0.020$ gives a luminosity distance, $D_L = 89.1$ Mpc and a distance modulus, $\mu = 34.75$ mag. The Milky Way extinction in the direction of SN 2019bkc is $E(B - V)_{MW} = 0.05$ mag (Schlafly & Finkbeiner 2011) with an assumed R_V of 3.1. We take $E(B - V)_{host} = 0$ mag due to the lack of obvious underlying host and lack of Na I D absorption lines. At $z = 0.02$, the absolute magnitude of any underlying host galaxy or globular cluster

would be fainter than $M_g \sim -10.1$ mag, $M_r \sim -10.9$ mag, and $M_z \sim -11.5$ mag, which is insufficiently deep to rule out most globular clusters (e.g. Lyman et al. 2016).

3. Light curves

The multi-colour photometry and colour curves of SN 2019bkc are shown in Fig. 2 and the calibrated photometry is presented in Table 2. The ATLAS non-detection and ZTF detection are less than 20 hours apart (0.80 d) but are separated by ~ 1 mag in brightness (albeit in different bands, ZTF-g and ATLAS-o). This suggests that the transient exploded some time close to the non-detection.

The LT g-band light curve rises to a peak on MJD 58546.9 $\pm$ 0.5, which is 5–6 d after the ZTF detection. The riz bands also peak around this time. The u-band is not observed on the rise, but from the earliest $ugriz$ SED we estimate a temperature of ~ 8700 K, which suggests that maximum light in the u-band occurred close to the first observation. We set our fiducial reference point throughout as the time of pseudo-bolometric maximum light, MJD 58546.02 $\pm$ 0.25 (see Sect. 3.2).

GROND observations at +4.24 d after pseudo-bolometric peak brightness provide the only detection in the NIR and show that the object was not NIR-bright – when the SED is fitted with a black body, no significant NIR excess is seen. NIR imaging from the LT with IO:I provided a non-detection in H with a limiting magnitude of >18.2 mag at +9.84 d. Further observations showed a decay rate of ~ 0.5 mag d^{-1} and a total decline of 3.4–4.8 mag in ~ 12 d across $griz$ with the redder bands decaying slower. Extrapolation of the g-band light curve gives $\Delta m_{15}(g) \sim 5$ mag.

The I-band light curve point of SN 2019bkc at +18 d after maximum from Chen et al. (2020) is consistent with a ^{56}Co tail. The absolute peak magnitudes and times for the luminosities in each band to decay by half their peak luminosity are given in Table 3.

3.1. Comparison of light curves

In Fig. 3, we compare the gri-band light curves of SN 2019bkc to those of various fast transients: the rapidly evolving SNe Ic 1994I (Richmond et al. 1994) and 2005ek (Drout et al. 2013), the Ca-rich events iPTF14gqr (De et al. 2018a), iPTF16hgs (De et al. 2018b), SN 2012hn (Valenti et al. 2014), and SN 2010et (Kasliwal et al. 2012), the rapidly evolving unexplained transients, SNe 2010X (Kasliwal et al. 2010) and 2002bj (Poznanski et al. 2010), and the unusual Ti-dominated OGLE-2013-SN-079 (Inserra et al. 2015). Figure 4 shows how extraordinarily fast the Δm_{15} decline of SN 2019bkc is in relation to other transients. SN 2019bkc has an incredibly fast decline, with the previously most rapidly declining objects SN 2005ek and SN 2010X seen to be significantly slower.

The light curves of the low-mass edge-lit double detonation (ELDD-L) model of a He-shell on the surface of a white dwarf from Sim et al. (2012) is also shown in Fig. 3. This model has a short rise time which match the early r and i light curves of SN 2019bkc but fails to replicate the g band. The model is also broader in i, cannot match the rapid decline seen in the three bands, and reaches the ^{56}Co decay tail earlier than SN 2019bkc.

Additionally, the shape of the light curve between the ATLAS-o non-detection and the ZTF-g band detection is of interest. We estimate the g-band upper-limit from the observed ATLAS-o band limit using the assumption that the underlying spectrum is a black body, which appears reasonable since the

Table 2. Optical and NIR photometry.

MJD	Band	Apparent magnitude	Facility
58546.02	u	18.1 ± 0.2	LT
58548.88	u	18.59 ± 0.07	LT
58546.02	g	17.74 ± 0.05	LT
58546.87	g	17.68 ± 0.02	LT
58548.88	g	17.89 ± 0.03	LT
58553.88	g	20.27 ± 0.04	LT
58554.86	g	20.85 ± 0.05	LT
58555.85	g	21.37 ± 0.08	LT
58556.85	g	21.4 ± 0.6	LT
58557.89	g	22.1 ± 0.4	LT
58559.03	g	22.4 ± 0.3	LT
58546.02	r	17.58 ± 0.05	LT
58546.87	r	17.54 ± 0.04	LT
58548.88	r	17.66 ± 0.03	LT
58553.88	r	19.59 ± 0.04	LT
58554.86	r	20.06 ± 0.03	LT
58555.85	r	20.69 ± 0.01	LT
58556.85	r	21.0 ± 0.2	LT
58557.89	r	21.1 ± 0.3	LT
58559.03	r	21.8 ± 0.3	LT
58564.87	r	>23.1	LT
58546.02	i	17.69 ± 0.03	LT
58546.87	i	17.68 ± 0.04	LT
58548.88	i	17.74 ± 0.02	LT
58553.88	i	19.55 ± 0.06	LT
58554.86	i	19.99 ± 0.03	LT
58555.85	i	20.42 ± 0.06	LT
58556.85	i	20.8 ± 0.1	LT
58559.03	i	21.5 ± 0.4	LT
58546.02	z	17.76 ± 0.04	LT
58546.87	z	17.71 ± 0.04	LT
58548.88	z	17.76 ± 0.02	LT
58553.88	z	19.22 ± 0.06	LT
58554.86	z	19.67 ± 0.05	LT
58555.85	z	20.09 ± 0.08	LT
58556.85	z	20.3 ± 0.1	LT
58557.89	z	20.7 ± 0.3	LT
58555.86	H	>18.2	LT
58559.06	g	22.4 ± 0.1	NTT
58559.06	r	21.8 ± 0.2	NTT
58559.06	i	21.5 ± 0.3	NTT
58559.06	z	21.1 ± 0.1	NTT
58550.26	g	18.41 ± 0.02	GROND
58550.26	r	17.95 ± 0.02	GROND
58550.26	i	18.00 ± 0.02	GROND
58550.26	z	17.95 ± 0.02	GROND
58550.26	J	18.55 ± 0.03	GROND
58550.26	H	18.76 ± 0.06	GROND
58550.26	K	>19.4	GROND
58540.45	o	>19.8	ATLAS
58544.43	o	17.9 ± 0.1	ATLAS
58548.42	o	17.5 ± 0.4	ATLAS
58552.41	o	18.7 ± 0.5	ATLAS
58556.40	o	20.2 ± 0.7	ATLAS

Table 3. Multi-colour light curve properties including the absolute magnitude at peak for each of the bands and the time for each light curve to decay to half its peak luminosity.

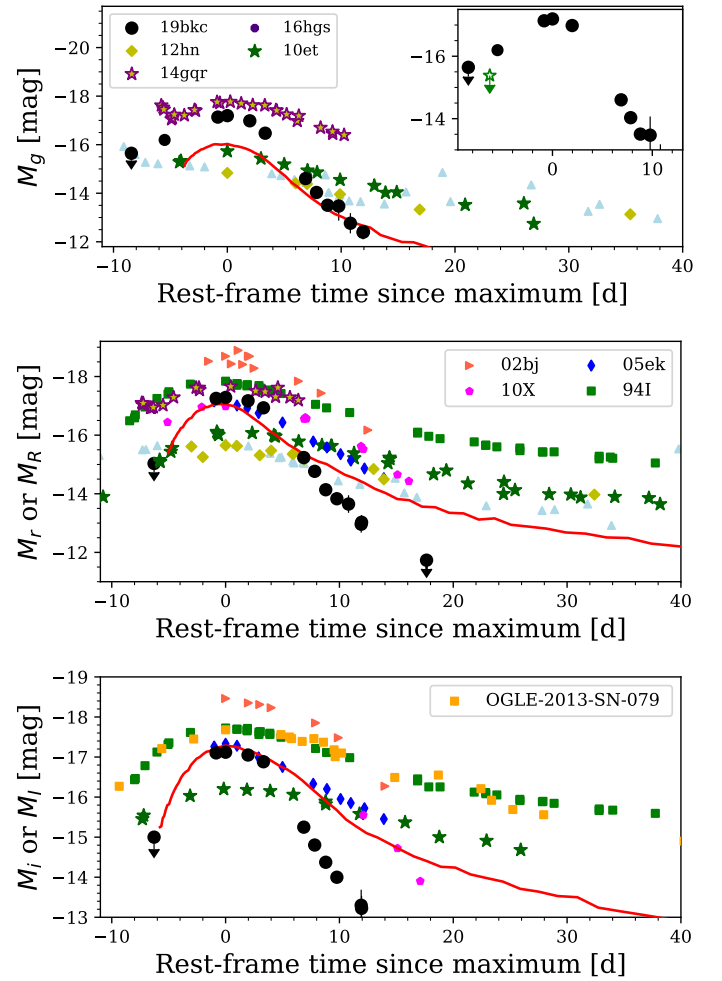| Band	M_{peak} [mag]	$t_{+1/2}$ [d]
u	−17.3 ± 0.1	−
g	−17.19 ± 0.02	3.8 ± 0.1
r	−17.33 ± 0.03	4.3 ± 0.1
i	−17.15 ± 0.05	4.4 ± 0.3
z	−17.09 ± 0.03	4.5 ± 0.4

Fig. 3. *Top*: g-band light curves of various fast transients; SN 2019bkc and the Ca-rich SNe 2010et, 2012hn, iPTF14gqr, and iPTF16hgs. The red line is the ELDD-L model from Sim et al. (2012). The inset shows the g band light curve with an estimated upper limit of 19.5 mag (green star) derived from the ATLAS-o band magnitude of 19.8 assuming the SED is a black body at ~20 000 K. *Middle*: r or R band light curves including SNe Ic 2005ek and 1994I, and the unusual transients SNe 2010X and 2002bj. *Bottom*: i or I band comparison with the addition of the Ti-dominated transient OGLE-2013-SN-079. The initial ATLAS-o non-detection is treated as if it was in r and i respectively.

spectrum at peak is still blue and relatively featureless. This results in a synthetic g magnitude limit of $19.8 > g > 19.1$ mag for temperatures in the range, $10^4 < T < 10^5$ K. At $T = 25\,000$ K the g limit is ~19.5 mag. The inset in the top panel of Fig. 3 shows that SN 2019bkc had a very sharp rise from non-detection to detection before levelling off, this is difficult to reconcile with a simple blast-wave approximation of $L \propto t^2$, and we note that the light curve of Ca-rich iPTF14gqr showed a double-peaked profile (De et al. 2018a).
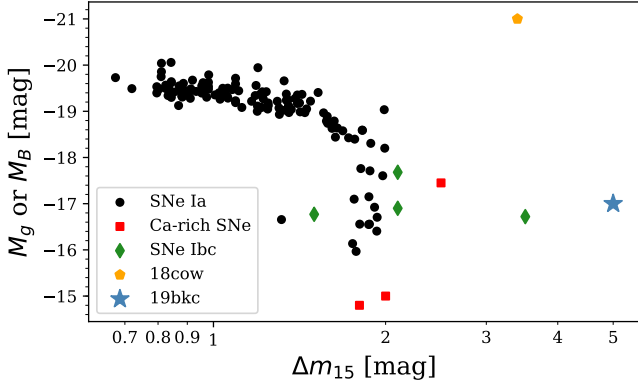
Fig. 4. Peak absolute magnitude in B or g as a function of decline rate for a selection of transients and SN 2019bkc. Differences in magnitude system and filter bandpass are negligible for the purpose of this plot which shows that the rapid decline of SN 2019bkc is unprecedented compared to the comparison objects. The SNe Ia data are from Galbany et al. (2019).

3.2. Pseudo-bolometric light curve

Figure 5 shows the *griz* (4000−10 000 Å) and *ugriz* (3000−10 000 Å) pseudo-bolometric light curves of SN 2019bkc, constructed following the method in Prentice et al. (2016). A simple polynomial fit to the light curve shows it reached a *griz* peak luminosity $L_p = (1.41 \pm 0.06) \times 10^{42}$ erg s^{-1} in 6.1 ± 0.4 d after the estimated explosion date, and *ugriz* peak of $(1.9 \pm 0.1) \times 10^{42}$ erg s^{-1} in 5.0 ± 0.4 d. The former is chosen to allow direct comparison with other objects, as this wavelength range encompasses the most commonly observed bands. The latter provides a better estimate of the bolometric luminosity by utilising all of the available photometry. A true bolometric light curve would encompass the UV to NIR, fortunately our *u*-band observations indicate that the peak of the SED of the transient is between *u* and *g* at our first epoch of multi-colour photometry. The derivatives of the two light curves at these times also suggest that we are not missing any significant contribution from the UV because in this case the light curves would show a steep decline. The absence of NIR photometry is harder to rectify, but in Prentice et al. (2016) it was found that the NIR flux over the range 10 000−24 000 Å is typically around 10% of the flux in 3000−10 000 Å at maximum light, for SE-SNe. GROND NIR observations a few days after the first epoch of multi-colour photometry show that this transient is not NIR bright. Thus, assuming that *u* captures the majority of the flux blueward of *g*, and taking a 10% NIR contribution, the peak bolometric luminosity could be expected to be in the region $\sim 2.2 \times 10^{42}$ erg s^{-1}.

The time for the *griz* light curve to decay by half its peak luminosity is 4.01 ± 0.04 d. SN 2019bkc reached a similar peak luminosity to ^{56}Ni-driven core-collapse events but approximately ten times lower than that of thermonuclear SNe Ia. A rise time from explosion to peak t_p of $\sim$5−6 d is short but not excessively so, and is similar to iPTF14gqr. However, its subsequent rapid decline is only rivalled by that of kilonova AT 2017gfo (e.g. Drout et al. 2017; Smartt et al. 2017), but the two are not spectroscopically similar.

3.2.1. Estimating M_{Ni}

On the assumption that the light curve peak is powered by ^{56}Ni decay (and excluding in this scenario the presence of short-lived radioisotopes), we use the analytical form of "Arnett's
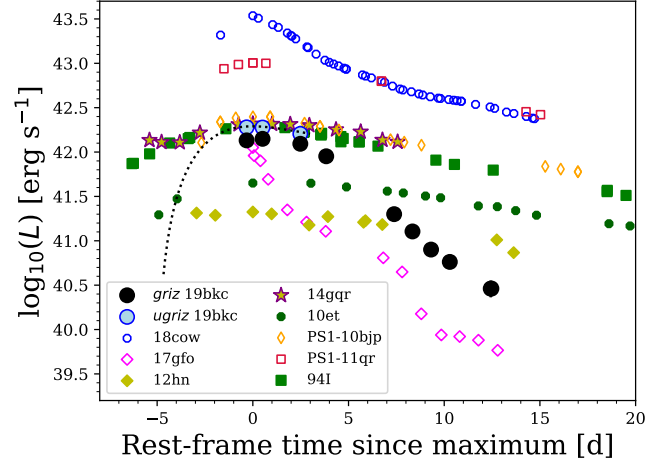
Fig. 5. *griz* (black solid circles) and *ugriz* (blue filled circles) pseudo-bolometric light curves of SN 2019bkc (black) shown in comparison to the *griz* pseudo-bolometric light curves of Type Ic SN 1994I (green), kilonova AT 2017gfo (Smartt et al. 2017), AT2018cow (Prentice et al. 2018a), and fast blue transients PS1-10bjp and PS1-11qr (Drout et al. 2014), Ca-rich SNe 2012hn (Valenti et al. 2014) and 2010et (Kasliwal et al. 2012), and "ultra-stripped" Ca-rich iPTF14gqr (De et al. 2018a). The dotted black line shows the best fit analytic ^{56}Ni powered light curve model of Valenti et al. (2008), fit to the *ugriz* bolometric light curve until 9 days after explosion.

rule" (Arnett 1982) as given in Stritzinger & Leibundgut (2005) to estimate the ^{56}Ni mass M_{Ni} required to give these peak luminosities

$$\frac{M_{Ni}}{M_{\odot}} = L_p \times \left(10^{43} \text{ erg s}^{-1}\right)^{-1}$$
$$\times \left(6.45 \times e^{-t_p/8.8} + 1.45 \times e^{-t_p/111.3}\right)^{-1}, \quad (1)$$

where L_p and t_p are the peak luminosity and rise-time respectively. For the *griz* bolometric light curve we take t_p to be 6.1 ± 0.4 and $L_p = (1.41 \pm 0.06) \times 10^{42}$ erg s^{-1}, which gives $M_{Ni} = 0.031 \pm 0.001\ M_{\odot}$. For the *ugriz* bolometric light curve we use $L_p = (1.9 \pm 0.1) \times 10^{42}$ erg s^{-1} and $t_p = 5.0 \pm 0.4$ d, this returns $M_{Ni} = 0.038 \pm 0.001\ M_{\odot}$. for the *griz* and *ugriz* luminosities, respectively. This method also assumes that the ^{56}Ni is located centrally, which may not be valid for this event (see Khatami & Kasen 2019), thus these values should be considered upper limits.

A simple model fit to the *ugriz* light curve, using the photospheric model of Valenti et al. (2008), is also shown in Fig. 5. The fit omits the ZTF detection, as per the discussion of the early light curve shape in Sect. 3.1. It extends to 9 days after explosion, after this time ejecta transparency leads to deviation between the observations and the model (see Valenti et al. 2008). The resulting physical parameters derived from the fits, $t_p = 4.8^{1.2}_{0.03}$ days and $M_{Ni} = 0.039^{0.003}_{0.001}\ M_{\odot}$ are consistent with that found above.

3.2.2. Estimating the ejecta mass

We also estimated the ejecta mass M_{ej} using the formulation given in Arnett (1982) and expressed as

$$M_{ej} = \frac{1}{2}\left(\frac{\beta c}{\kappa}\right)\tau_m^2 v_{sc} \quad (2)$$

where $\beta \approx 13.7^{0.1}_{3.4}$ is dimensionless factor which varies for different density profiles (Arnett 1980, 1982), τ_m is a timescale of

the light curve model which can be approximated by the rise time, v_{sc} is a scale velocity which we take to be a measured line velocity around maximum light, and κ is a constant optical opacity.

The choice of κ has some bearing on the value of M_{ej} as calculated in Eq. (2). Although taken as a constant in various model light curves, the actual optical opacity varies with time (e.g. Chugai 2000; Nagy 2018), but tests have shown that that a constant opacity can be a reasonable assumption at early times (see Mazzali et al. 2000; Taddia et al. 2018). SN 2019bkc is a H/He-deficient SN, so to select an appropriate value for κ, we search the literature literature and consider only SNe of this type. For SNe Ia, where the large abundance of Fe-group elements is a source of significant opacity, Cappellaro et al. (1997) used $\kappa = 0.15\,\mathrm{cm^2\,g^{-1}}$, while Arnett (1982) used $\kappa = 0.08\,\mathrm{cm^2\,g^{-1}}$. The light curve of the broad lined SNe Ic 1997ef was modelled in Mazzali et al. (2000) using the same code as Cappellaro et al. (1997), this time a lower constant opacity of $0.08\,\mathrm{cm^2\,g^{-1}}$ was used owing to the lower Fe abundance in this SN type. The average opacity of model CC-SNe light curves was investigated by Nagy (2018), where it was found that $\kappa = 0.1\,\mathrm{cm^2\,g^{-1}}$ was suitable for their H/He-deficient models. Taddia et al. (2018) demonstrated that fitting the light curves of H-deficient CC-SNe with a simple analytical model and a constant opacity $\kappa = 0.07\,\mathrm{cm^2\,g^{-1}}$ returned physical parameters consistent with more complex hydrodynamic light curve models. Prentice et al. (2019) also found that using $\kappa = 0.07\,\mathrm{cm^2\,g^{-1}}$ gave comparable ejecta masses to both photospheric phase and nebular phase spectroscopic modelling of H-deficient CC-SNe, with the exception of some gamma-ray burst SNe. From Sect. 5 we find that the outer ejecta is not rich in Fe-group elements, and there is no indication of helium. From the early-nebular spectra in Sect. 4.2 we see no indication of strong Fe II or Fe III line emission, demonstrating that the ejecta is poor in Fe-group elements relative to normal SNe Ia and is more like H/He-deficient CC-SNe. This justifies the use of $\kappa = 0.07\,\mathrm{cm^2\,g^{-1}}$, but to show the range of possible M_{ej}, we consider the range 0.07–$0.1\,\mathrm{cm^2\,g^{-1}}$.

Thus, using the values and uncertainties associated with β and κ, along with the *ugriz* pseudo-bolometric rise time of $5.0 \pm 0.4\,\mathrm{d}$ and a scale velocity $v_{sc} = 14\,500 \pm 500\,\mathrm{km\,s^{-1}}$ from the Si II $\lambda\,6355$ line (see Sect. 4), we find $M_{ej} = 0.4^{+0.1}_{-0.2}\,M_\odot$.

4. Spectroscopy

Spectra of SN 2019bkc were taken over a 20 day period covering from shortly before maximum light until well into the decay phase (Fig. 6). The epochs that spectra were taken at are denoted with respect to the light curve in Fig. 2. The initial spectra appeared photospheric but there was a rapid evolution to an optically thin "nebular regime", beginning at just 13 d post maximum. Analysis of the unusual late-time velocity shifts is presented in Sect. 4.2, while modelling of the photospheric phase spectra is performed in Sect. 5.

4.1. Photospheric phase spectra

The first spectra around maximum light are blue with broad, shallow absorption features in the range of 6000–7000 Å, with these features becoming narrower between our $-0.1\,\mathrm{d}$ and $+0.8\,\mathrm{d}$ spectra (top panel of Fig. 6). We identify the blueward feature as Si II $\lambda\,6355$ (for the redward feature, we tentatively suggest Ar II, see Sect. 5) at a velocity of $\sim -15\,000\,\mathrm{km\,s^{-1}}$. One day later, $+0.8\,\mathrm{d}$ after maximum, the Si II velocity has decreased

to $\sim -13\,000\,\mathrm{km\,s^{-1}}$ and the redward feature of the two has weakened. Two days later, the spectra are still blue but less so than previously seen and the Si II absorption line profile with $v \sim -10\,000\,\mathrm{km\,s^{-1}}$ appears to have narrowed, while the feature to the red of it is very weak. There is evidence of P-Cygni-like emission from the Ca II NIR triplet at 3.1 d. Absorption by the O I $\lambda 777$ lines may be obscured by atmospheric O_2 absorption, which occurs in the 7441–7509 Å region when corrected for $z = 0.02$. This corresponds with oxygen blueshifts of 10 000–13 000 $\mathrm{km\,s^{-1}}$.

By $+5.1\,\mathrm{d}$, the spectrum of SN 2019bkc is substantially different. The 6000–7000 Å features have given way to a single feature centred on the Si II line, which is broader with an absorption minimum at $v \sim -11\,000\,\mathrm{km\,s^{-1}}$, slightly greater than that measured a few days before. This broadening of absorption lines and "plateau" of the measured line velocities was also see in SN 2012hn (Valenti et al. 2014). This spectrum at this time shows remarkable similarity to SNe Ic spectra 0–10 d after maximum light, as is shown in Fig. 7. Unlike SNe Ic, the spectra of SN 2019bkc show considerable complexity in the region blueward of ~5000 Å with a series of broad features within which there are narrower features. These features are not just noise, and the inset of Fig. 6 shows how this region evolves from $+2.8\,\mathrm{d}$ to $+5.1\,\mathrm{d}$, which covers the period the object was observed with the NTT. Two absorption features at 4900 Å and 5010 Å are seen and show no significant velocity evolution during the three observations (~2.3 d). These two features have a similar wavelength difference as Fe II $\lambda\lambda$ 4924, 5018. If we hypothetically attribute the absorption to these lines then the measured expansion velocity would be $\sim -1000\,\mathrm{km\,s^{-1}}$, which is significantly lower than the $\sim -11\,000\,\mathrm{km\,s^{-1}}$ measured for the Si II line. There is no indication of a feature associated with the much stronger Fe II λ 5169 line however, which suggests that the wavelength difference is coincidental. Additionally, if this line is associated with the two absorption features then there is nothing which coincides with the rest of the Fe II lines, making this association unlikely.

We have taken this investigation a step further however. Comparison of the $+5.1\,\mathrm{d}$ spectrum with those of SN 1994I between maximum light and $+10\,\mathrm{d}$ in Fig. 7 shows a curious offset between the region dominated by Fe-group elements (<5500 Å) and the intermediate mass elements (IME). In SN 1994I, the line profiles in the region 4000–5400 Å at these epochs are attributable to Fe II, Mg I, Ti II (Sauer et al. 2006). If the features were to be formed by the same line transitions in SN 2019bkc then they are some $8000\,\mathrm{km\,s^{-1}}$ slower than in SN 1994I, effectively at rest. This contrasts with the lines formed by IMEs – Si II λ 6355, O I λ 7772, and the Ca II NIR triplet – which are seen at a higher velocity in SN 2019bkc. This would require that the line forming region of the Fe group elements is below that of the IMEs, contrary to what is seen in SNe Ic (Prentice & Mazzali 2017).

Finally, a low S/N spectrum was obtained with the LT less than three days later at $+7.7\,\mathrm{d}$ after maximum light. Very little can be obtained from this spectrum other than it shows no obvious signs of [Ca II] and Ca II emission lines, which appear strong within two to three weeks of maximum in SNe Ic.

4.2. The extraordinary Ca-rich early nebular phase

We obtained two X-shooter spectra at $+12.9$ and $+19.6\,\mathrm{d}$ after maximum covering the near-UV through NIR wavelengths, the UV and optical spectra are shown in the bottom panel of Fig. 4 and the NIR spectra in Fig. 8. Both optical spectra show a flux
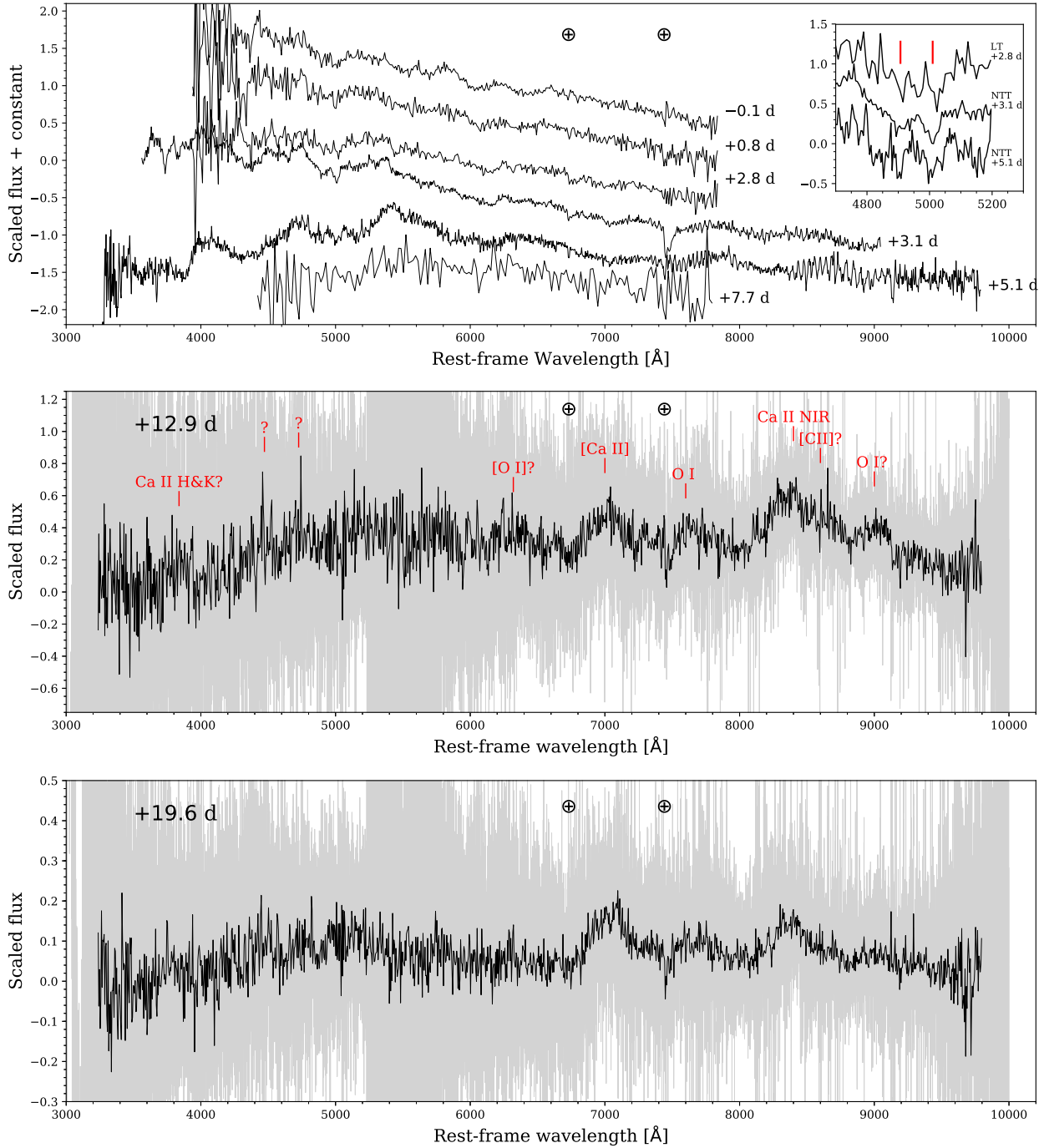
Fig. 6. *Top*: optical spectra from LT:SPRAT and NTT:EFOSC2. The phases are with respect to maximum light. The inset highlights some narrow features in the spectra that remain unidentified. *Middle and bottom*: raw VLT:X-shooter UV and optical spectra (light grey) and binned to 5 Å (black). The outer edges of the UVB and VIS arms have been omitted from the binning process due to excess noise. Note that the region between 5200 and 5800 Å is the inner boundary between the UVB and VIS arms. Due to the low signal to noise ratio (S/N) any features here are unlikely to be real.

excess above the continuum level in the range of 4500–6000 Å, which becomes more prominent in the later spectrum. They also show three evolving emission lines at ~7000, 7700, and 8400 Å, and possibly three at 3838 Å, 4472 Å, and 4726 Å. The NIR spectra on these days are noisy and somewhat featureless when telluric features are accounted for, with the only line being an absorption around ~11 200 Å. This feature remains unexplained as there are no obvious lines in this aside from [Fe II] in this region, but these do not result in absorption, see Fig. 8.

The positioning of the optical emission features between 6500 and 8800 Å is difficult to reconcile with the rest wavelength of any strong emission line that is commonly seen in SNe. The most probable candidates for the 7000 Å feature are blueshifted [Fe II] λ 7155 and [Ca II] $\lambda\lambda$ 7921, 7324. These lines are seen in the nebular phase spectra of most types of SNe, with the former being prominent in the spectra of SNe Ia, but less so in CC-SNe (see Jerkstrand et al. 2014; Mazzali et al. 2015). In Fig. 6 it can be seen that the 7000 Å feature is prominent, and is at least
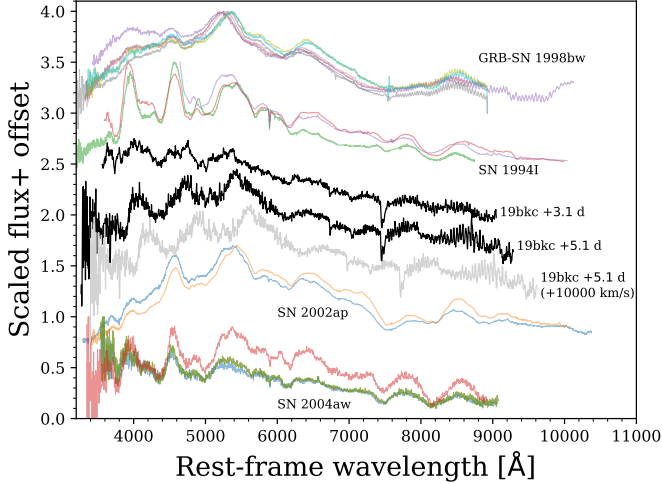
Fig. 7. SN 2019bkc +3.1 d and +5.1 d spectra compared with a sample of SNe Ic (data from Patat et al. 2001; Filippenko et al. 1995; Foley et al. 2003; Modjaz et al. 2014). The comparison objects are shown at phases from 0 to +10 d after maximum light. There are similarities between SN 2019bkc and these objects, especially in the +5.1 d spectrum. Without our nebular spectra this transient could have been considered a peculiar type Ic. Also plotted is the rest-frame +5.1 d spectrum red-shifted 10 000 km s^{-1} (grey). This now poorly matches the comparison SNe, especially in the regions redward of 7000 Å. It demonstrates that the earlier spectra are likely not affected by whatever process causes the velocity shifts in the nebular spectra and that a redshift significantly lower than $z = 0.02$ is incompatible.
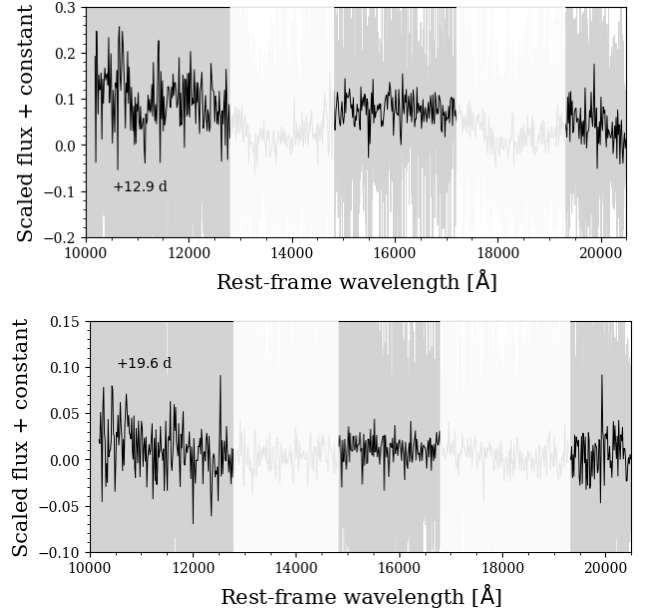

Fig. 8. X-shooter NIR spectra at phases +12.9 d (*top*, grey) and +19.6 d (*lower*, grey) and the binned spectra (black). Regions with telluric absorption have been masked.

as strong as any emission blueward of it. If it were to be dominated by the Fe II λ 7155 transition then it could be expected that the region around 4000–5000 Å would be dominated by strong [Fe II] and [Fe III] lines, as in SNe Ia (Mazzali et al. 2015, 2018). In instances where the [Fe II] λ7155 is comparable to the flux in the blueward region, emission by forbidden calcium dominates the spectrum in this region (Jerkstrand et al. 2014, 2015). This argument leads to the conclusion that the ~7000 Å feature is dominated by [Ca II] $\lambda\lambda$ 7921, 7324.

In the region around 8400 Å the strongest nebular emission lines in SNe are associated with Ca II $\lambda\lambda$ 8498, 8542, 8662, [Fe II] λ 8617, [Fe II] λ 8892, and [C I] λ 8727. The [Fe II] emissions typically dominates in SNe Ia (Mazzali et al. 2011), but is either absent, or present as an equal component in CC-SNe (Mazzali et al. 2010; Jerkstrand et al. 2015). As argued previously, the lack of strong iron lines elsewhere in the ejecta suggests that this feature is principally composed of the Ca II NIR triplet.

These apparent calcium-dominated features are considerably blueward of the respective emission rest-wavelengths. However, if a redshift of ~10 000 km s^{-1} from the rest-frame is applied to the spectra then the main emission lines align with those seen in Ca-rich transients (bottom panel of Fig. 9), which correspond with [Ca II] $\lambda\lambda$ 7291, 7324, O I λ 7772, the Ca II NIR. There are also two weaker features that may be [C II] λ 8727 (Perets et al. 2010) and OI λ 9263 (Jerkstrand et al. 2015). If these identifications are correct, the former is blueshifted by ~4000 km s^{-1} and the latter by ~9000 km s^{-1}. Additionally, if O I λ 7774 and O I λ 9263 are present then this may also suggest the presence of O I λ 8446 within the 8400 Å feature, although this is not typically identified in models of nebular spectra.

In the blue, the apparent emission line at ~3838 Å could be Ca II H&K blueshifted by 10 000 km s^{-1}. The two remaining

features around 4472 Å and 4726 Å remain unidentified as we find no line that is positioned at these wavelengths in the rest frame or with a velocity of $\sim -10\,000$ km s^{-1}. A final point on the line identification is that, for all the lines transitions and possible blends considered, the observed features require a significant blueshift from any of their rest-wavelengths. The velocity shifts are discussed further in Sect. 4.3.

Given that the nebular spectra imply that SN 2019bkc belongs to the diverse family of Ca-rich transients, in the top panel of Fig. 9 we compare its photospheric spectra with four Ca-rich events: SN 2012hn (Valenti et al. 2014), SN 2005E (Perets et al. 2010), SN 2010et (Kasliwal et al. 2012), iPTF16hgs (De et al. 2018b), as well as the "ultra-stripped SN" iPTF14gqr (De et al. 2018a) . The best spectroscopic match is to iPTF14gqr (at +7.2 and +10.96 d). We can find no good match with the other objects, even when we adjust the spectra of SN 2019bkc over the redshifts within the galaxy group ($z = 0.018-0.022$). We do note there is significant heterogeneity in the Ca-rich spectra, with SN 2012hn being a clear outlier in terms of appearance, where there is no indication of the apparent He I features seen in iPTF16hgs or SN 2010et.

The lower panel of Fig. 9 shows the +12.9 and +19.6 d spectra of SN 2019bkc compared to the same sample of Ca-rich nebular phase spectra, with the addition of PTF12bho (Lunnan et al. 2017). The emission lines at ~7000 and ~8400 Å seen in the spectra of SN 2019bkc look similar to those seen in the Ca-rich events (and associated with [Ca II] and Ca II, respectively). However, the [Ca II] and Ca II lines in SN 2019bkc display a significant blueshift of ~10 000 km s^{-1} compared to the rest wavelength of these features, which is discussed in Sect. 4.3. The +19.6 d spectrum, corrected for this offset velocity, is shown in Fig. 9 in grey and the peaks of the Ca features are seen to agree much more closely with the other objects after this correction.

4.3. Velocity shifts

Figure 10 shows the nebular-phase spectra centred on the positions of Ca II λ 8662 NIR, [Ca II] λ 7324 and O I λ 7772
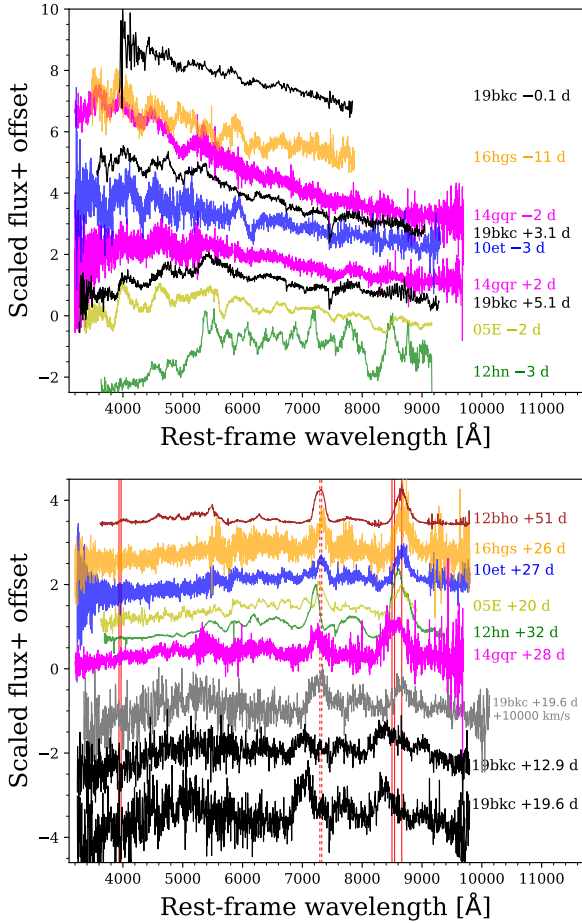
Fig. 9. *Top*: photospheric spectra of SN 2019bkc compared with the Ca-rich transients SN 2012hn, SN 2005E, iPTF16hgs, SN 2010et, and "ultra-stripped SN" iPTF14gqr. The spectra at this phase are heterogeneous and SN 2019bkc is most similar to iPTF14gqr. *Lower*: nebular phase spectra of SN 2019bkc compared with the same transients plus PTF12bho. Ca II and [Ca II] lines are denoted in red solid and dashed lines respectively. To match the +19.6 d spectrum of SN 2019bkc to that of SN 2005E requires a velocity shift of ~10 000 km s^{-1} (grey).

in rest-frame velocity space for SN 2019bkc compared to SN 2012hn and SN 2010et. SN 2019bkc shows a blueshift in both the [Ca II] and Ca II features, with an offset of ~10 000 km s^{-1} from their rest-frame positions. A blueshift in the [Ca II] line in the range of 3500–5000 km s^{-1} was previously identified for SN 2012hn (Valenti et al. 2014). As seen in Fig. 10, the spectra of SN 2010et are consistent with no discernible blueshift, while the lines of SN 2012hn appear blueshifted ~4000 km s^{-1}. Foley (2015) investigated velocity shifts in the [Ca II] lines of 13 Ca-rich events and found velocity shifts of up to 1700 km s^{-1} but nothing close to the ~ −10 000 km s^{-1} identified for SN 2019bkc here.

The right hand panel of Fig. 10 shows that there is no evidence of velocity evolution in the Ca II NIR line between the two observations. The relative position of this emission line in other Ca-rich transients and the rest-frame wavelength of the NIR triplet here gives a velocity offset of ~ −10 500 km s^{-1}, which we adopt as the typical velocity shift. Alternatively, aligning [Ca II] λ 7324 with the red peak of the observed line gives a velocity of ~ −12 000 km s^{-1} at +12.9 d and ~ −10 000 km s^{-1} at +19.6 d, which are consistent with the Ca II NIR velocity offset.

In both SN 2019bkc and SN 2012hn there is a feature in the form of a broad emission "bump" between [Ca II] and Ca II NIR. Valenti et al. (2014) do not attribute this emission to anything in particular but its position is consistent with O I λ7772. Emission from this line is seen in the early nebular phases of H-deficient core-collapse SNe, so we continue on the assumption that the feature is due primarily to O I λ 7772 and measure a velocity shift in the region of −8000 to −10 000 km s^{-1} for this line. At redder wavelengths, we have identified a feature at ~9000 Å that may be O I λ 9263 (Jerkstrand et al. 2015). If the identification of O I λ 9263 is correct, then the velocity shift would be ~ − 9000 km s^{-1}, which would be in rough agreement with the velocity of the assumed O I λ 7772 line. This would suggest the O I -emitting region is also located at a similar velocity to the Ca-emitting regions. No double-peaked profile is identified for the O I feature but the region is strongly contaminated by a strong telluric feature ~ − 11 000 km s^{-1} from 7772 Å.

Finally, we have excluded dust as being responsible for the velocity offset. In circumstances involving absorption by dust, the red wing of a symmetric emission profile is suppressed, leading to a line that is peaked blueward of the rest wavelength. Here, the extreme velocity shift observed would require the original emission lines to have a full width half maximum of ~20 000 km s^{-1}, suggesting it is very unlikely that dust is causing this velocity offset to the blue.

4.4. Estimating [Ca II]/[O I]

Calculating the ratio of [Ca II] to [O I] line strength is a common analytical tool for Ca-rich transients to show how strong the [Ca II] line is compared with that in core-collapse (CC) SNe. In previous Ca-rich SNe, the [O I] λλ 6300, 6363 line appeared several tens of days after maximum light (Valenti et al. 2014; Milisavljevic et al. 2017). In Fig. 6 it appears as if there may be emission features around ~6300 Å in the +12.9 and +19.6 d spectra. However, on investigation these are found not to be significantly above the noise level of the spectra, thus we conclude there is no clear emission from [O I]. This may be because the spectra are too early, even accounting for the rapid evolution of the light curve, or that the S/N is just too poor.

We estimate an upper limit to the [O I] flux by assuming that the line is present and accounts for the entirety of the flux in a region approximated by a Gaussian with the same width as that of the [Ca II] λ 7291 line. Measurements were taken at two velocity offsets; 0 km s^{-1} and the velocity measured for the [Ca II] of −10 000 km s^{-1}. For the +12.9 d spectrum these upper limits gave [Ca II]/[O I] >5.4 and >5.4, respectively, and for +19.6 d they were >14.1 and >10.8. The similarity in the values supports the argument that the observable "features" in the spectra at ~6300 Å are not real.

Figure 11 demonstrates that with these upper-limits, SN 2019bkc sits within the Ca-rich region of the [Ca II]/[O I] parameter space and well outside that of CC events where the ratio is typically <1−2 (Valenti et al. 2014; Milisavljevic et al. 2017; Nicholl et al. 2019). [O I] is not seen in normal SNe Ia but has been detected in one subluminous event (Taubenberger et al. 2013).

SN 2019bkc displays an absence of [O I] and a 1:1 ratio of [Ca II]/Ca II. In SNe Iax, this has been attributed to a high-density environment (Jha et al. 2006; McCully et al. 2014). However, SNe Ibc typically have a [Ca II]/Ca II ratio of ~ 1:1 but with stronger [O I] emission in the early nebular phase. The He-shell detonation models of Dessart & Hillier (2015) are also strong in
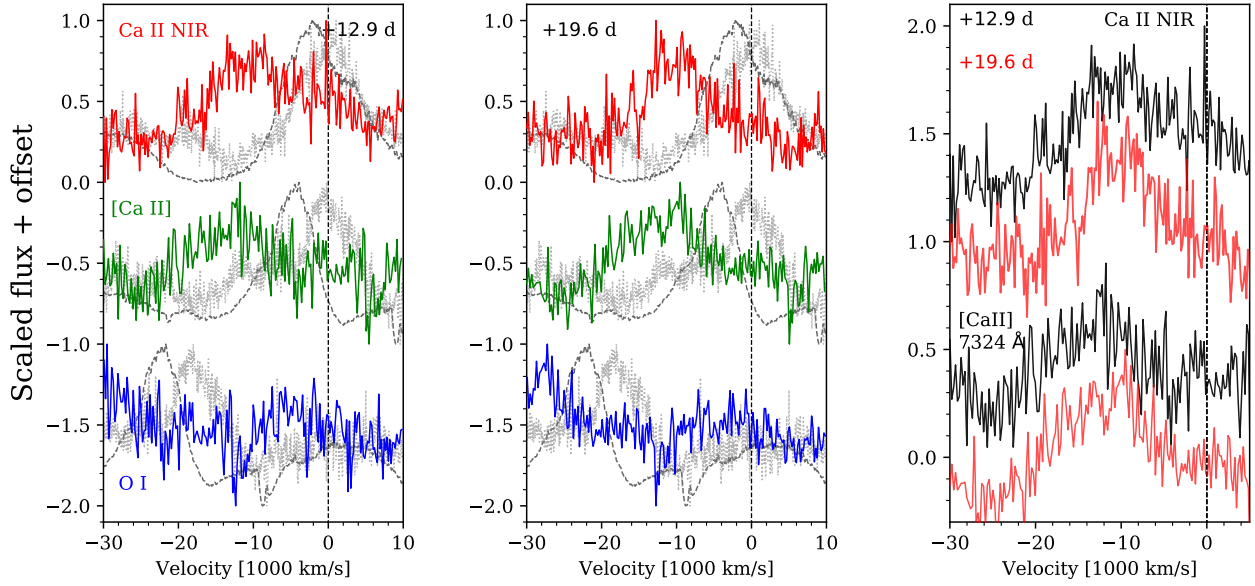
Fig. 10. *Left and centre*: spectra of SNe 2019bkc (line), 2012hn (black dashed), and 2010et (grey dotted) centred in velocity space on the rest position of Ca II NIR (red), [Ca II] λ 7324 (green), and O I λ 7772 (blue) respectively for +12.9 d (*left*) and +19.6 d (*centre*). A telluric feature is present in the O I feature at $\sim$11 000 km s^{-1} and the peaks at $-23\,000$ and $-18\,000$ km s^{-1} for SNe 2012hn and 2010et, respectively, are the [Ca II] features located to the blue of this O I feature. *Right*: Ca II NIR (top) and [Ca II] (bottom) lines plotted in sequence for the two epochs. The Ca II NIR triplet is consistent with no velocity evolution, while the [Ca II] line appears to decrease in velocity. Given the S/N of the spectrum this may not be real.

Ca II and weak in [O I] due to a very low oxygen mass. The nebular spectra of SN 2005E showed [O I] emission at $\sim$2 months after explosion. Nebular modelling of these phases reveals that oxygen is $\sim$13% of the total ejecta mass (Perets et al. 2010). In the case of SN 2019bkc, it may be too early for the [O I] line to have developed due to the high density of the ejecta at this phase or it may be that the ejecta is intrinsically oxygen deficient.

5. Spectral modelling

We model the photospheric phase spectra at -0.1, +3.1 d, and 5.1 d with a Monte-Carlo 1D radiative transfer code (Mazzali & Lucy 1993; Lucy 1999; Mazzali et al. 2000). This code has previously been used to model SNe Ia (e.g. Mazzali et al. 2014; Ashall et al. 2014), stripped-envelope SNe (e.g. Mazzali et al. 2017; Prentice et al. 2018b), and the Ca-rich event SN 2005E (Waldman et al. 2011). The model spectra on Waldman et al. (2011) used the results of He detonation models, specifically an explosion model of 0.45 $M_\odot$ CO core with a 0.2 $M_\odot$ He envelope. The resultant model spectra were seen to be rich in narrow Ti II lines and weak in Si II lines.

The approach taken here is somewhat different as we have assumed no specific origin for this object (e.g. white dwarf, massive star). Rather than produce model spectra for a pre-determined explosion profile, we start with a density profile and attempt to match the shape of spectra of SN 2019bkc at three epochs as best as possible by varying the luminosity L. The time since explosion ($t - t_{\rm exp}$) is also a key parameter in the model and fortunately, the explosion time of SN 2019bkc is very well constrained by our non-detection ($t_{\rm exp} = MJD58540.9 \pm 0.4$). Following the approach of previous works (e.g. Sauer et al. 2006; Prentice et al. 2018b), we then aimed to match the line velocities and the features present by varying the photospheric velocity, $v_{\rm ph}$, and the abundance of elements above the photosphere.
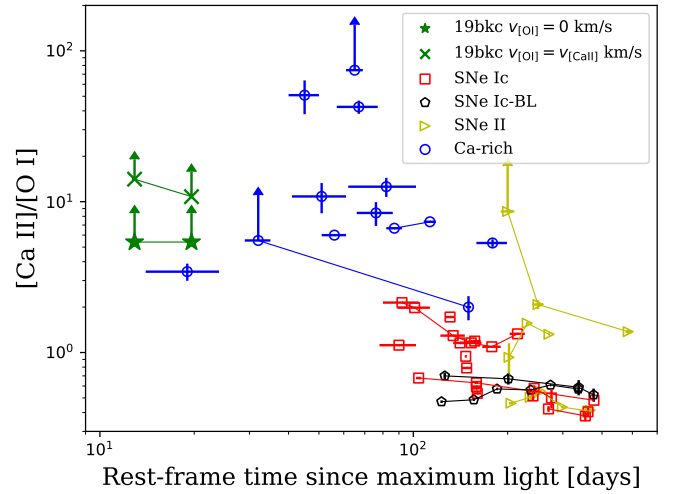

Fig. 11. Ratio of [Ca II] $\lambda\lambda$ 7291, 7324 to [O I] $\lambda\lambda$ 6300, 6363 for a sample of core-collapse SNe and Ca-rich events; the ratio is significantly larger in Ca-rich objects. SN 2019bkc is shown in green calculated for two velocity positions, 0 km s^{-1} and if it has the same offset as the [Ca II] and Ca II lines. Ancillary data from Valenti et al. (2014).

The observed spectra were absolute flux calibrated using the available photometry and corrected for $E(B-V)_{\rm MW}$ and the assumed redshift of $z = 0.02$. The distance to the object is not well constrained due to the affects of peculiar motions within the cluster on the actual redshift of SN 2019bkc. We used a distance modulus of 34.71 mag as stated in Sect. 2.2, but note that as $T \propto L^{1/4} \propto D_L^{1/2}$, then the distance uncertainty adds an additional uncertainty to the model parameters.

Given the similarity of some of the early spectra to SNe Ic, the density profile used for the models is CO21, which was used to model type Ic SN 1994I (Nomoto et al. 1994; Iwamoto et al. 1994; Sauer et al. 2006) This density profile has $M_{\rm ej} \sim 1\,M_\odot$ and

$E_k \sim 1 \times 10^{51}$ erg. SN 2019bkc has a rise time approximately half that of SN 1994I, so in order to match the spectral evolution of SN 2019bkc, the CO21 density profile was scaled in mass to give total masses of 0.8, 0.6, 0.4, and $0.2\,M_\odot$. Only for the latter two mass models did the density drop sufficiently fast with time to form the spectra with an acceptable photospheric velocity, temperature, and luminosity at the appropriate epochs. Of these two models, the lowest mass density profile $M_{ej} \sim 0.2\,M_\odot$ provided marginally better models. The mass scaling preserves the specific kinetic energy E_k/M_{ej}, giving this model $E_k \sim 2 \times 10^{50}$ erg. Thus, from the models we find that $M_{ej} = 0.2-0.4\,M_\odot$, consistent with the mass derived from the pseudo-bolometric light curve using Eq. (2), and with $E_k = 2-4 \times 10^{50}$ erg and $E_k/M_{ej} \sim 1$ (in units of $[10^{51}\,\text{erg}]/[M_\odot]$).

We assumed that the ejecta is completely defined by this model setup and did not include a He envelope as used by Waldman et al. (2011). The lack of He lines in the observed spectra suggests that either He is not present or the conditions are not right to non-thermally excite the He present (Lucy 1991). In the latter case we cannot rule out some dynamical effect on the ejecta from transparent He.

5.1. −0.1 d spectrum

The −0.1 d ($t - t_{exp} = 5.0$ d) spectrum is approximately at maximum light. The SPRAT spectrum does not extend blueward of ~4000 Å, so to constrain the blueward part of the model we calculated a synthetic u-band using the LT SDSS-u filter profile and match the spectrum to the dereddened photometry. This spectrum (Fig. 12) is modelled with a photospheric velocity of 14 500 km s^{-1} and a black body temperature, $T_{bb} \sim 11\,000$ K. We find that the spectra are much better represented with the heavier elements found in the Waldman et al. (2011) abundance distributions than those for SNe Ic, where the vast majority of the ejecta is C and O with only trace Fe-group elements. The main features in the bluest part of the model spectra are produced by Fe III, Ti II. Although Ti II lines are present they do not contribute significantly to line formation in any region of the observed spectrum. These elements make up ~4% of the abundance distribution for this model. The broad double feature between 6000 and 6600 Å is replicated on the blue side by Si II $\lambda\,6355$ and a series of Ar II lines, mainly Ar II $\lambda\lambda\,6638$, 6639, 6643, on the red side. For the latter, C II $\lambda\,6580$ was found to appear too far blueward and the absence of a significant contribution from He I $\lambda\,5876$ to the spectrum rules out He I $\lambda\,6678$. Importantly, Ar constitutes 1−10% of the ejecta in the Waldman et al. (2011) He detonation model, and 10% in this model, but it is not present in abundance distributions of SNe Ic (see Sauer et al. 2006; Mazzali et al. 2017).

5.2. +3.1 d spectrum

The +3.1 d ($t - t_{exp} = 8.2$ d) spectrum is the first observed with the NTT and is the first to extend blueward of 4000 Å. This spectrum has a higher S/N and resolution compared with the earlier spectra and extends to shorter wavelengths. It also shows a degree of complexity not seen in "normal" Type I events due to the number of features at wavelengths shorter than 5400 Å. The model spectrum has $T_{bb} \sim 9300$ K and a photospheric velocity of 10 500 km s^{-1}. The last u-band observation was 0.3 d prior to this at ~18.6 mag. The synthetic u calculated from the model is ~30% dimmer than the extrapolated value, which itself has an uncertainty of at least 10%. This may suggest that the
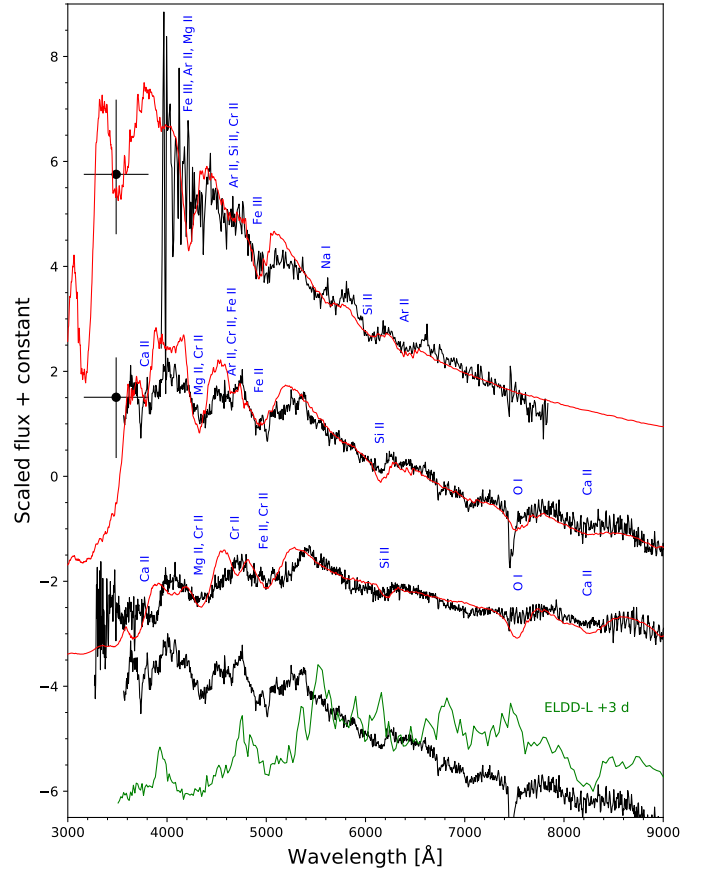

Fig. 12. Spectroscopic modelling of SN 2019bkc (red) using a density profile with $M_{ej} \sim 0.2\,M_\odot$ and $E_k \sim 2 \times 10^{50}$ erg compared with observed spectra at −0.1, +3.1, and +5.1 d (black). Prominent elements are noted along with the u-band fluxes used to constrain the models. Also included is the scaled ELDD-L model spectrum from Sim et al. (2012) (green) at ~3 d after maximum compared to our spectra of SN 2019bkc at a similar phase.

temperature needs to be higher to increase the model flux in this region, or that the quantity of Fe-group elements needs to be reduced to decrease the effect of line-blanketing. Such changes would affect the model spectrum in the observed region but without knowledge of the actual spectrum in the u-band region the kind of fine tuning required to investigate this further cannot be performed.

Despite the presence of Ar as 10% of the ejecta above the photosphere at this phase, the Ar II lines seen in the earlier spectra are not replicated, which is consistent with the evolution of the ~6400 Å feature in the observed spectra. As before, the features in the blue side of the spectrum are predominately formed from Ca II H&K, Mg II, Ti II, Ti II, and now Fe II rather than Fe III oweing to the lower temperature. On the red side of the spectrum we see more lines formed from IMEs, Si II $\lambda\,6355$, O I $\lambda\,7772$, and Ca II NIR. The strength and position of the O I line is ambiguous however, owing to contamination by the O_2 telluric feature. The abundance of Fe-group elements in the model at this phase is ~4%, the majority of which is ^{56}Ni and Cr and ~1% Fe and Ti.

5.3. +5.1 d spectrum

The +5.1 d ($t - t_{exp} = 10.2$ d) spectrum was modelled with a photospheric velocity of 7500 km s^{-1} and $T_{bb} \sim 8300$ K. At this

Table 4. Comparison of model properties.

Model	Progenitor	$M_{\rm ej}$ [$M_\odot$]	$E_{\rm k}$ [erg]	$E_{\rm k}/M_{\rm ej}$ [10^{51} erg]/[$M_\odot$]	Reference
2019bkc	–	0.2–0.4	2–4×10^{50}	~1	This work
CO.45He.2[†]	White dwarf	0.65	1.8×10^{50}	~0.3	(Waldman et al. 2011)
ELDD-L	White dwarf	0.66	~6×10^{50}	~0.9	(Sim et al. 2012)
iPTF14gqr	Massive star	0.2	~2×10^{50}	~1	(De et al. 2018a)

Notes. [†]This model was used to create synthetic spectra which were then compared with SN 2005E in Waldman et al. (2011). The nebular phase spectra of SN 2005E were modelled in Perets et al. (2010) and gave an ejecta mass of ~0.3 $M_\odot$.

phase the model is producing narrow lines while those in the spectrum are broader, which suggests that the slope of the density profile above the photosphere boundary at this point should be flatter (i.e. the line forming region more extended) than we have used. This behaviour is especially unusual however, as broad lines are seen to give way to narrower lines in normal SNe. Also, as noted in Sect. 4, this spectrum is rather peculiar, as the Si II line is broader and at a higher velocity than earlier. It was also noted that, when compared with SN 1994I, the velocity of features associated with Fe-group elements in the blue are apparently well below that of the IME velocities in the red. We see that this is not reflected in the model spectrum, the IME lines form at too low a velocity, while that of the Fe-group lines is too high. As a consequence, the model cannot recreate the redward extent of the blue wing of the pseudo-emission peak at ~5500 Å. The IME line velocities could be better replicated by increasing the total mass of the model used, which would allow the photosphere to form at a larger velocity co-ordinate (as a test, setting $v_{\rm ph} = 10\,500\,{\rm km\,s^{-1}}$ proved to position these lines well), but this adversely affects other aspects of the model. Firstly, it would further increase the velocity of the line-forming regions of the Fe-group elements, then to conserve the flux within the spectrum (and therefore the luminosity), the temperature would have to decrease which may lead to problems in matching the spectral shape. Additionally, these affects would be seen in the earlier two models. The difficulty in finding a model to match the spectrum at this phase suggests that the structure of the ejecta is complex, and it must be stressed that the spectra are effectively nebular <7 d after this observation so this spectra may not be fully photospheric, which is a requirement of the model setup.

5.4. Comparison of model properties

In Table 4 the properties derived from the spectroscopic models of SN 2019bkc are compared with the He-detonation CO.45He.2 explosion model of Waldman et al. (2011) and the low-mass edge-lit double-detonation explosions model EDDL-L of Sim et al. (2012), both of which are modelled from CO white dwarf progenitors with a He envelope. We also compare with the ultra-stripped model of De et al. (2018a), which is of core-collapse origin.

The total ejecta mass for our model of SN 2019bkc is smaller by a factor of ~2 compared with the two white dwarf explosion models, but is similar to that for the "ultra-stripped" model. The specific kinetic energy is most similar to the "ultra-stripped" model at ~1 and is marginally larger compared with ELDD-L but is larger by a factor of ~0.3 compared with CO.45He.2. These results marginally favour a massive star progenitor. However, we tentatively detected Ar II in the spectra, which is in agreement with the abundance profile of CO.45He.2 and is perhaps

the strongest evidence for a white-dwarf progenitor. This is further supported by the difficulty obtaining a suitable model spectrum using a stripped-envelope SN-like abundance, although we note that the abundance distribution used is weaker in Fe-group elements (especially Ti) compared with CO.45He.2/ELDD-L (Waldman et al. 2011; Sim et al. 2012). Consequently, we cannot say for certain that our results favour one scenario over another.

6. Discussion

SN 2019bkc has shown itself to be rather unusual in several ways, from the rapidly declining light curve and early spectra with similarities to normal type Ic SNe to the high velocity shift of ~10 000 km s^{-1} seen in the [Ca II], Ca II and O I features in the nebular spectra. We now discuss possible explanations for its physical appearance and the environment that hosts it.

6.1. Explaining the blueshifted calcium emission lines

Shifts in the central positions of emission lines are seen in the late-time spectra of SNe Ia with values in the range of ±2000 km s^{-1} (e.g. Maeda et al. 2010; Maguire et al. 2018). Velocity offsets in forbidden lines of Ca and O have also been identified in Type Ib/c SNe but the magnitudes of the shifts are significantly lower with values of up to ~1000 km s^{-1} (Taubenberger et al. 2009). The Ca-rich transient sample studied to date showed velocity offsets in their [Ca II] features with respect to their rest-frame positions ranging from zero to 5000 km s^{-1} and have been seen as both redshifts and blueshifts (Valenti et al. 2014; Foley 2015). However, the blueshifts seen in the [Ca II] and Ca II emission lines of SN 2019bkc of ~10 000 km s^{-1} are the highest seen to date in any Ca-rich event and we tentatively identify a similar blueshift in the O I 7772 Å feature. In this section, we discuss some scenarios to explain these extreme velocity shifts.

6.1.1. SN 2019bkc as an asymmetric explosion

A very asymmetric explosion is a potential way to explain the large velocity shifts seen in the nebular phase spectra of SN 2019bkc, with the Ca-rich (and O-rich) ejecta, or perhaps ^{56}Ni ejecta with trace amounts of Ca and O, ejected towards us at high velocity. The velocity shift measured is the *minimum* total velocity, this is in the case of the asymmetry being directly towards us. Any other viewing angle increases the total velocity, which increases the kinetic energy without increasing the mass, so the specific kinetic energy increases. If the remnant is a compact object then momentum could be conserved without the need for mass ejected in the opposing direction, which we see no evidence of. Asymmetry also affects the observed light curve in

both duration and peak magnitude (e.g. Sim et al. 2007; Barnes et al. 2018). If the explosion was significantly asymmetric this could explain the rapidly declining light curve through a reduction in the photon diffusion time and the velocity shift seen in the nebular spectra. The main argument against this model is that the photospheric-phase spectra are inconsistent with any significant velocity shift when compared with other objects, see Fig. 7 and the emitting region at early times appears symmetric.

Alternatively, an asymmetric explosion gives an asymmetric distribution of elements. 3D explosion models of core-collapse SNe have shown that explosions happen through symmetry breaking in the gain region, low pressure regions at the gain layer allow shocked material pass through and unbind the star. The result of this process is plumes of material being ejected (Wongwathanarat et al. 2013; Summa et al. 2018). If the radioactive material synthesised in the explosion was preferentially ejected as a "blob" moving $\sim 10\,000\,\mathrm{km\,s^{-1}}$ then the nebular emission could be explained by the radioactive material exciting the material around it. It also explains the fast light curve on the basis of reduced photon diffusion time as the column density above the material is greatly reduced of the centrally-located case. This simplistic explanation is not without its own problems, however, as it requires no radioactive elements anywhere else in the ejecta as there is no emission at velocities significantly away from $\sim 10\,000\,\mathrm{km\,s^{-1}}$. The underlying explosion scenario resulting in this type of ejecta structure is also unexplained.

6.1.2. SN 2019bkc as an extreme line-of-sight motion object

Ca-rich transients have a preference for remote locations far from the centres of their host galaxies. This has been confirmed by Frohmaier et al. (2018) not to be a selection affect due to the setup of transient surveys but something intrinsic to the explosions. It has been suggested that Ca-rich events result from systems that have previously been kicked from the centre of their host galaxies by interaction with a central supermassive black hole (SMBH; Foley 2015). A potential correlation was identified between the offset from the likely host galaxy and the velocity offset seen in the [Ca II] emission lines, with less offset objects displaying larger velocity offsets. If we assume that the most likely host galaxy for the object is the brightest cluster galaxy, NGC 3090 at an offset distance of 95 kpc from SN 2019bkc, then it was predicted it should have a velocity offset roughly consistent with zero. However, it has the highest offset seen to date for a Ca-rich event of $\sim 10\,000\,\mathrm{km\,s^{-1}}$ and does not fit in this picture. Even if it was associated with 2dFGRS TGN216Z084 (galaxy "B" in Fig. 1) at a redshift of 0.019, it would have a separation of 34 kpc.

Milisavljevic et al. (2017) also discussed that if interaction with a SMBH was responsible for the velocity offset seen in the Ca features then it should also be seen in the O features and typically this is not the case, but our results suggest this may be the case for SN 2019bkc where a potential O I feature blueshifted by $8000-10\,000\,\mathrm{km\,s^{-1}}$ may be present. Coughlin et al. (2018) has explored the kick velocities that would be expected for systems interacting with SMBH and found that some systems could have velocities greater than $10\,000\,\mathrm{km\,s^{-1}}$. This in an attractive solution for the velocity offset in the nebular phase but is inconsistent when applied to explain the photospheric phase spectra that do not require a velocity offset. Therefore, we conclude that this scenario is unlikely to explain the properties of SN 2019bkc.

6.2. Explosion scenarios for SN 2019bkc

The analysis presented so far has not resulted in a firm identification of a particular explosion scenario or progenitor for SN 2019bkc. In this section we discuss possible progenitor scenarios and the pros and cons for each.

6.2.1. SN 2019bkc as a double-detonation event

In Fig. 2, we compared SN 2019bkc to a low-luminosity edge-lit double-detonation model (ELDD-L) of a sub-Chandrasekhar mass white dwarf by Sim et al. (2012). Even compared to this extreme model, the light curve of SN 2019bkc is still significantly faster and bluer in its $g-r$ colour. The model spectra of the ELDD-L model at 8 d past maximum are shown alongside our models in Fig. 12. The spectrum peaks at $\sim 5500\,\text{Å}$ and is defined by copious narrow absorption features, mostly Ti II and Ca II. This is not unlike the model spectra produced from the explosion models given in Waldman et al. (2011). Comparison with our spectra at similar phases, however, shows very few similarities. Our spectra peak towards 4000 Å, and while there are several unidentified narrow features in the blue the spectrum has a strong continuum and is rather sparse of features blueward of 6000 Å.

6.2.2. SN 2019bkc as a tidal disruption event by an intermediate-mass black hole

There have been suggestions of a link between Ca-rich events and the tidal disruption of a white dwarf by an intermediate mass black holes (IMBH; e.g. Luminet & Pichon 1989; Rosswog et al. 2009; Sell et al. 2015). A prediction of white dwarf-IMBH tidal disruption models is that a thermonuclear explosion can be triggered during the disruption that can produce a low-luminosity optical transient (Rosswog et al. 2009; Clausen & Eracleous 2011; MacLeod et al. 2014, 2016) and if the impact parameter is relatively low then the ejecta may be Ca-rich (Kawana et al. 2018; Anninos et al. 2018). The burning efficiency, however, may be too low to produce Ca in large quantities and depends on how much is required to explain the late-time spectra of Ca-rich transients.

Other predictions of white dwarf and IMBH tidal disruption models are that there should be soft X-ray emission resulting from the accretion disk and potentially X-ray emission from a relativistic jet (MacLeod et al. 2016). Emission from a relativistic jet is strongly viewing angle dependent and is not expected to be visible in all cases. The X-ray emission from the accretion disk, however, should be visible from any viewing angle and is expected to have a luminosity of $\sim 10^{41}-10^{43}\,\mathrm{erg\,s^{-1}}$ that last for months to a year after the event. A handful of Ca-rich events have been searched for X-ray signatures but no high-energy counterpart has been identified to date (e.g. Sell et al. 2015, 2018). Our *Swift* XRT upper limit of $<6.3 \times 10^{40}\,\mathrm{erg\,s^{-1}}$ was obtained $\sim 42\,\mathrm{d}$ after explosion, which would rule out most of the model range for X-ray emission from an accretion disk for SN 2019bkc.

These models also predict strong viewing angle dependencies in the observed optical properties due to a bulk orbital motion (MacLeod et al. 2016). It is predicted that the absorption profiles in the photospheric phase could have an additional offset of up to $10\,000\,\mathrm{km\,s^{-1}}$ to bluer or redder wavelengths. This is not seen in the early spectra of SN 2019bkc that were found through spectral modelling to be consistent with a stripped envelope SN or an unusual thermonuclear event with no velocity

offset needing to be applied. The line velocity shifts were only seen in the nebular-phase spectra and this is not explained by the bulk orbital motion scenario in tidal disruption event of a white dwarf by an IMBH.

6.2.3. SN 2019bkc as a merger between a white dwarf and neutron star or stellar-mass black hole

Metzger (2012) modelled the merger of a white dwarf with a neutron star or stellar mass black hole and looked at the resulting properties of the accretion disk. The observables include a light curve that rises to a peak on a timescale of ~5 days before decaying rapidly, reaching peak bolometric luminosities of $10^{39}-10^{41.5}\,\mathrm{erg\,s^{-1}}$, and an ejecta that contains Ar with a total ejecta mass is between 0.3 and 1 $M_\odot$ and ejecta velocities $\sim 10^4\,\mathrm{km\,s^{-1}}$. The properties of the explosion model are similar to the observed SN 2019bkc, especially through the light curve, although SN 2019bkc is more luminous at $10^{42.3}\,\mathrm{erg\,s^{-1}}$. The argument against this model is that the ejecta is Ca-deficient and so couldn't explain the later appearance of [Ca II] and Ca II NIR. Ca is an efficient coolant however, and would give rise to these lines even if small amounts were present in the ejecta of such a merger.

6.2.4. SN 2019bkc as an ultra-stripped SN

Ultra-stripped SNe (Tauris et al. 2013) arise from the core-collapse of massive He stars that have been stripped of virtually all the material above their Chandrasekhar-mass core through binary interaction with a companion, most likely a neutron star. The low ejecta mass of a few 0.1 $M_\odot$ and low E_k of $1 \times 10^{50}-1 \times 10^{51}$ erg leads to dim, rapidly evolving light curves as the M_{Ni} synthesised is a few 0.01 $M_\odot$, the diffusion time is short (Tauris et al. 2015; Moriya et al. 2017). The pre-explosion abundance structure should be rich in the elements produced in stellar nucleosynthesis; He, C, O, Mg, Ca, Si, S. At core-collapse most of this material is left unburnt and contributes to spectroscopic line formation.

De et al. (2018a) interpreted iPTF14gqr as an ultra-stripped type Ic SN. The spectra of this object and SN 2019bkc have many similarities, including the nebular-phase spectra that are undoubtedly Ca-rich in appearance and unlike those more usually seen in SNe Ic where the [O I] $\lambda\lambda$ 6300, 6363 line dominates. In terms of the light curve, SN 2019bkc is much faster, but the overall colour evolution and temperature evolution are not too dissimilar. iPTF14gqr had a double peaked light curve, interpreted as shock-cooling from recently ejected He-rich material from the companion star. Comparatively, we inferred that the early g-band light curve of SN 2019bkc showed a steep rise and a rapid levelling off. There is no evidence of He in the spectra of SN 2019bkc, although this may be because spectral observations began too late. The results of our spectroscopic modelling can neither confirm nor deny that this transient is an ultra-stripped SNe. Aside from the possible presence of Ar at early times the model still remains viable for a CC event.

However, the explosion of a massive star apparently so far from a star-forming region is much harder to explain with a CC event. Assuming that the life time of the progenitor star is <40 Myr (Tauris et al. 2015) and that the host is the nearby elliptical galaxy NGC 3090, then this object must have travelled at least ~95 kpc in this time, placing a lower limit on the velocity of ~2300 km s^{-1}. If the progenitor system was not ejected immediately, and has any radial velocity component, then this velocity must be significantly higher. It also stands to reason that this requires NGC 3090 to have had some star formation in the recent past in order to produce a NS/He-star binary system.

7. Conclusions

In this work, we present the discovery, observations, and analysis of the extraordinary Ca-rich transient ATLAS19dqr/SN 2019bkc. The event took place in the intracluster space of a galaxy group with $z \sim 0.02$. There is no source underlying the transient in pre-explosion DECaLS images ruling out the presence of a faint host or globular cluster at approximately $M > -10$ mag.

A robust non-detection 0.8 d prior to the first observation reveals a short rise, while the multi-colour light curves show a clear peak at ~ -17 mag approximately 5–6 d after the non-detection. These components give a light curve shape that is not consistent with a blast-wave approximation to the luminosity. The light curves then begin a remarkably rapid decline, with $\Delta m_{15}(g) \sim 5$ mag, making SN 2019bkc one of the most rapidly evolving transients known. A pseudo-bolometric light curve constructed from $ugriz$ photometry reached a peak luminosity of $L_p = (1.9 \pm 0.1) \times 10^{42}\,\mathrm{erg\,s^{-1}}$ in 5.0 ± 0.4 d, giving $M_{\mathrm{Ni}} = 0.038 \pm 0.001\,M_\odot$.

The spectroscopic observations proved to be equally unusual. In the photospheric phase we find similarities to SNe Ic but with considerable complexity in the spectra in the form of weak and narrow features blueward of 5500 Å. In the late photospheric phase (+5.1 d) we see an unusual situation with indications of high velocity IMEs but low velocity Fe-group elements. There is evidence of an increase in line velocity and line broadening in the Si II λ 6355 line at these times. The nebular phase spectra display strong lines which we identify to be [Ca II] $\lambda\lambda$ 7291, 7324 and Ca II NIR, but with a measured blueshift of 10 000–12 000 km s^{-1}. Assuming that the peak of the emission line defines the velocity then we see a change in [Ca II] velocity from $v = 12\,000$ km s^{-1} on day +12.9 to $v = 9500$ km s^{-1} on day +19.6. The velocity of the Ca II NIR line remains unchanged.

There is no detection of [O I] λ6300, 6363 at either the rest wavelength or ~10 000 km s^{-1} in the nebular spectra. Consequently we measure only upper limits for the flux of this line and the resulting [Ca II]/[O I] ratio places the object firmly in the region occupied by Ca-rich transients. We speculate that the object may be O-deficient, or the ejecta density may be too high and so it may be too early for the line to appear.

Three photospheric phase spectra were modelled using a 1D radiative transfer code and reveal a low ejecta mass of $M_{\mathrm{ej}} \sim$ 0.2–0.4 $M_\odot$ (consistent with $0.4^{+0.1}_{-0.2}\,M_\odot$ calculated from the light curve), and $E_k \sim (2-4) \times 10^{50}$ erg. Abundance profiles for SNe Ic (Sauer et al. 2006; Mazzali et al. 2017) and He-detonation models (Waldman et al. 2011) were used as a starting basis for defining the input abundance of the models. We find that the early spectra are mostly IMEs with ~3–4% as a combination of ^{56}Ni, ^{56}Fe, Ti, Cr at velocities >14 000 km s^{-1}. A broad absorption feature, which is present in the earliest two spectra can be explained by a combination of Ar II lines along the abundances found in the Waldman et al. (2011) explosion models. We note difficulties in modelling the +5.1 d spectrum due to the odd velocity profile. The tentative detection of an Ar II line in the maximum light spectrum marginally preferences a thermonuclear explosion (possibly a He detonation) over a explosion of CC origin. However, with a low ejecta mass and specific kinetic energy of the ejecta $E_k/M_{\mathrm{ej}} \sim 1$ [10^{51} erg]/$M_\odot$, it is more similar to ultra-stripped Ca-rich iPTF14gqr than models of He-detonation and double-detonation events.

SN 2019bkc was a highly unusual event with one of the fastest ever light curve decline rate for an extragalactic transient. It has been our hope that as we find more Ca-rich transients, we will better understand their nature. In particular, thanks to the extreme velocity shift seen in the early nebular lines this object has added to the overall diversity and now the picture seems less clear. Our results show that the transient cannot be conclusively attributed to a massive star or white dwarf progenitor and more detailed modelling of the nebular-phase spectra, in particular, is required to identify the most likely explosion scenario.

References

Ahn, C. P., Alexandroff, R., Allende Prieto, C., et al. 2012, ApJS, 203, 21
Anninos, P., Fragile, P. C., Olivier, S. S., et al. 2018, ApJ, 865, 3
Arnett, W. D. 1980, ApJ, 237, 541
Arnett, W. D. 1982, ApJ, 253, 785
Ashall, C., Mazzali, P., Bersier, D., et al. 2014, MNRAS, 445, 4427
Barnes, J., Duffell, P. C., Liu, Y., et al. 2018, ApJ, 860, 38
Bellm, E. C., Kulkarni, S. R., Graham, M. J., et al. 2019, PASP, 131, 018002
Buzzoni, B., Delabre, B., Dekker, H., et al. 1984, The Messenger, 38, 9
Cappellaro, E., Mazzali, P. A., Benetti, S., et al. 1997, A&A, 328, 203
Chen, P., Dong, S., Stritzinger, M. D., et al. 2020, ApJ, 889, L6
Chen, T.-W., Inserra, C., Fraser, M., et al. 2018, ApJ, 867, L31
Chugai, N. N. 2000, Astron. Lett., 26, 797
Clausen, D., & Eracleous, M. 2011, ApJ, 726, 34
Colless, M., Dalton, G., Maddox, S., et al. 2001, MNRAS, 328, 1039
Coughlin, E. R., Darbha, S., Kasen, D., & Quataert, E. 2018, ApJ, 863, L24
De, K., Kasliwal, M. M., Ofek, E. O., et al. 2018a, Science, 362, 201
De, K., Kasliwal, M. M., Cantwell, T., et al. 2018b, ApJ, 866, 72
Dessart, L., & Hillier, D. J. 2015, MNRAS, 447, 1370
Dey, A., Schlegel, D. J., Lang, D., et al. 2019, AJ, 157, 168
Drout, M. R., Soderberg, A. M., Mazzali, P. A., et al. 2013, ApJ, 774, 58
Drout, M. R., Chornock, R., Soderberg, A. M., et al. 2014, ApJ, 794, 23
Drout, M. R., Piro, A. L., Shappee, B. J., et al. 2017, Science, 358, 1570
Faber, S. M., Wegner, G., Burstein, D., et al. 1989, ApJS, 69, 763
Filippenko, A. V., Barth, A. J., Matheson, T., et al. 1995, ApJ, 450, L11
Foley, R. J. 2015, MNRAS, 452, 2463
Foley, R. J., Papenkova, M. S., Swift, B. J., et al. 2003, PASP, 115, 1220
Freudling, W., Romaniello, M., Bramich, D. M., et al. 2013, A&A, 559, A96
Frohmaier, C., Sullivan, M., Maguire, K., & Nugent, P. 2018, ApJ, 858, 50
Galbany, L., Ashall, C., Höflich, P., et al. 2019, A&A, 630, A76
Gal-Yam, A. 2017, in Observational and Physical Classification of Supernovae, eds. A. W. Alsabti, & P. Murdin, 195
Gal-Yam, A., Mazzali, P. A., Manulis, I., & Bishop, D. 2013, PASP, 125, 749
Greiner, J., Bornemann, W., Clemens, C., et al. 2008, PASP, 120, 405
Hinshaw, G., Larson, D., Komatsu, E., et al. 2013, ApJS, 208, 19
Inserra, C., Sim, S. A., Wyrzykowski, L., et al. 2015, ApJ, 799, L2

Iwamoto, K., Nomoto, K., Höflich, P., et al. 1994, ApJ, 437, L115
Jerkstrand, A., Smartt, S. J., Fraser, M., et al. 2014, MNRAS, 439, 3694
Jerkstrand, A., Ergon, M., Smartt, S. J., et al. 2015, A&A, 573, A12
Jha, S., Branch, D., Chornock, R., et al. 2006, AJ, 132, 189
Kasliwal, M. M., Kulkarni, S. R., Gal-Yam, A., et al. 2010, ApJ, 723, L98
Kasliwal, M. M., Kulkarni, S. R., Gal-Yam, A., et al. 2012, ApJ, 755, 161
Kawana, K., Tanikawa, A., & Yoshida, N. 2018, MNRAS, 477, 3449
Khatami, D. K., & Kasen, D. N. 2019, ApJ, 878, 56
Kraft, R. P., Burrows, D. N., & Nousek, J. A. 1991, ApJ, 374, 344
Krühler, T., Küpcü Yoldaş, A., Greiner, J., et al. 2008, ApJ, 685, 376
Lucy, L. B. 1991, ApJ, 383, 308
Lucy, L. B. 1999, A&A, 345, 211
Luminet, J., & Pichon, B. 1989, A&A, 209, 103
Lunnan, R., Kasliwal, M. M., Cao, Y., et al. 2017, ApJ, 836, 60
Lyman, J. D., James, P. A., Perets, H. B., et al. 2013, MNRAS, 434, 527
Lyman, J. D., Levan, A. J., Church, R. P., Davies, M. B., & Tanvir, N. R. 2014, MNRAS, 444, 2157
Lyman, J. D., Levan, A. J., James, P. A., et al. 2016, MNRAS, 458, 1768
MacLeod, M., Goldstein, J., Ramirez-Ruiz, E., Guillochon, J., & Samsing, J. 2014, ApJ, 794, 9
MacLeod, M., Guillochon, J., Ramirez-Ruiz, E., Kasen, D., & Rosswog, S. 2016, ApJ, 819, 3
Maeda, K., Taubenberger, S., Sollerman, J., et al. 2010, ApJ, 708, 1703
Maguire, K., Sim, S. A., Shingles, L., et al. 2018, MNRAS, 477, 3567
Margalit, B., & Metzger, B. D. 2016, MNRAS, 461, 1154
Mazzali, P. A., & Lucy, L. B. 1993, A&A, 279, 447
Mazzali, P. A., Iwamoto, K., & Nomoto, K. 2000, ApJ, 545, 407
Mazzali, P. A., Maurer, I., Valenti, S., Kotak, R., & Hunter, D. 2010, MNRAS, 408, 87
Mazzali, P. A., Maurer, I., Stritzinger, M., et al. 2011, MNRAS, 416, 881
Mazzali, P. A., Sullivan, M., Hachinger, S., et al. 2014, MNRAS, 439, 1959
Mazzali, P. A., Sullivan, M., Filippenko, A. V., et al. 2015, MNRAS, 450, 2631
Mazzali, P. A., Sauer, D. N., Pian, E., et al. 2017, MNRAS, 469, 2498
Mazzali, P. A., Ashall, C., Pian, E., et al. 2018, MNRAS, 476, 2905
McCully, C., Jha, S. W., Foley, R. J., et al. 2014, ApJ, 786, 134
Metzger, B. D. 2012, MNRAS, 419, 827
Milisavljevic, D., Patnaude, D. J., Raymond, J. C., et al. 2017, ApJ, 846, 50
Modigliani, A., Goldoni, P., Royer, F., et al. 2010, in Observatory Operations: Strategies, Processes, and Systems III, Proc. SPIE, 7737, 773728
Modjaz, M., Blondin, S., Kirshner, R. P., et al. 2014, AJ, 147, 99
Morgan, W. W., Kayser, S., & White, R. A. 1975, ApJ, 199, 545
Moriya, T. J., Mazzali, P. A., Tominaga, N., et al. 2017, MNRAS, 466, 2085
Mulchaey, J. S., Kasliwal, M. M., & Kollmeier, J. A. 2014, ApJ, 780, L34
Nagy, A. P. 2018, ApJ, 862, 143
Nicholl, M., Berger, E., Blanchard, P. K., Gomez, S., & Chornock, R. 2019, ApJ, 871, 102
Nomoto, K., Yamaoka, H., Pols, O. R., et al. 1994, Nature, 371, 227
Oke, J. B. 1990, AJ, 99, 1621
Patat, F., Cappellaro, E., Danziger, J., et al. 2001, ApJ, 555, 900
Perets, H. B., Gal-Yam, A., Mazzali, P. A., et al. 2010, Nature, 465, 322
Piascik, A. S., Steele, I. A., Bates, S. D., et al. 2014, in Ground-based and Airborne Instrumentation for Astronomy V, Proc. SPIE, 9147, 91478H
Poznanski, D., Chornock, R., Nugent, P. E., et al. 2010, Science, 327, 58
Prentice, S. J., & Mazzali, P. A. 2017, MNRAS, 469, 2672
Prentice, S. J., Mazzali, P. A., Pian, E., et al. 2016, MNRAS, 458, 2973
Prentice, S. J., Maguire, K., Smartt, S. J., et al. 2018a, ApJ, 865, L3
Prentice, S. J., Ashall, C., Mazzali, P. A., et al. 2018b, MNRAS, 478, 4162
Prentice, S. J., Ashall, C., James, P. A., et al. 2019, MNRAS, 485, 1559
Pursiainen, M., Childress, M., Smith, M., et al. 2018, MNRAS, 481, 894
Richmond, M. W., Treffers, R. R., Filippenko, A. V., et al. 1994, AJ, 107, 1022
Rosswog, S., Ramirez-Ruiz, E., & Hix, W. R. 2008, ApJ, 679, 1385
Rosswog, S., Kasen, D., Guillochon, J., & Ramirez-Ruiz, E. 2009, ApJ, 705, L128
Sauer, D. N., Mazzali, P. A., Deng, J., et al. 2006, MNRAS, 369, 1939
Schlafly, E. F., & Finkbeiner, D. P. 2011, ApJ, 737, 103
Sell, P. H., Maccarone, T. J., Kotak, R., Knigge, C., & Sand, D. J. 2015, MNRAS, 450, 4198
Sell, P. H., Arur, K., Maccarone, T. J., et al. 2018, MNRAS, 475, L111
Shen, K. J., Kasen, D., Weinberg, N. N., Bildsten, L., & Scannapieco, E. 2010, ApJ, 715, 767
Sim, S. A., Sauer, D. N., Röpke, F. K., & Hillebrandt, W. 2007, MNRAS, 378, 2
Sim, S. A., Fink, M., Kromer, M., et al. 2012, MNRAS, 420, 3003
Smartt, S. J., Valenti, S., Fraser, M., et al. 2015, A&A, 579, A40
Smartt, S. J., Chen, T.-W., Jerkstrand, A., et al. 2017, Nature, 551, 75
Smith, K. W., Williams, R. D., Young, D. R., et al. 2019, Res. Notes Am. Astron. Soc., 3, 26

Steele, I. A., Smith, R. J., Rees, P. C., et al. 2004, in Ground-based Telescopes, ed. J. M. Oschmann, Jr., Proc. SPIE, 5489, 679

Stritzinger, M., & Leibundgut, B. 2005, A&A, 431, 423

Suh, H., Yoon, S.-C., Jeong, H., & Yi, S. K. 2011, ApJ, 730, 110

Summa, A., Janka, H.-T., Melson, T., & Marek, A. 2018, ApJ, 852, 28

Taddia, F., Stritzinger, M. D., Bersten, M., et al. 2018, A&A, 609, A136

Taubenberger, S., Valenti, S., Benetti, S., et al. 2009, MNRAS, 397, 677

Taubenberger, S., Kromer, M., Pakmor, R., et al. 2013, ApJ, 775, L43

Tauris, T. M., Langer, N., Moriya, T. J., et al. 2013, ApJ, 778, L23

Tauris, T. M., Langer, N., & Podsiadlowski, P. 2015, MNRAS, 451, 2123

Tonry, J. L., Denneau, L., Heinze, A. N., et al. 2018, PASP, 130, 064505

Tonry, J., Denneau, L., Heinze, A., et al. 2019, Transient Name Server Discovery Report, 310

Valenti, S., Benetti, S., Cappellaro, E., et al. 2008, MNRAS, 383, 1485

Valenti, S., Yuan, F., Taubenberger, S., et al. 2014, MNRAS, 437, 1519

Vernet, J., Dekker, H., D'Odorico, S., et al. 2011, A&A, 536, A105

Waldman, R., Sauer, D., Livne, E., et al. 2011, ApJ, 738, 21

Wongwathanarat, A., Janka, H.-T., & Müller, E. 2013, A&A, 552, A126

Woosley, S. E., & Kasen, D. 2011, ApJ, 734, 38

Yuan, F., Kobayashi, C., Schmidt, B. P., et al. 2013, MNRAS, 432, 1680

[1] School of Physics, Trinity College Dublin, The University of Dublin, Dublin 2, Ireland
e-mail: sipren.astro@gmail.com

[2] Astrophysics Research Centre, School of Mathematics and Physics, Main Physics Building, Queen's University Belfast, Belfast, County Antrim BT7 1NN, UK

[3] Max-Planck-Institut für Astrophysik, Karl-Schwarzschild-Straße 1, 85748 Garching bei München, Germany

[4] European Southern Observatory, Karl-Schwarzschild-Straße 2, 85748 Garching bei München, Germany

[5] Physik-Department, Technische Universität München, James-Franck-Straße 1, 85748 Garching bei München, Germany

[6] School of Physics & Astronomy, Cardiff University, Queens Buildings, The Parade, Cardiff CF24 3AA, UK

[7] Institute of Cosmology and Gravitation, University of Portsmouth, Portsmouth PO1 3FX, UK

[8] Max-Planck-Institut für Extraterrestrische Physik, Giessenbachstraße 1, 85748 Garching, Germany

[9] European Southern Observatory, Alonso de Córdova 3107, Casilla 19, Santiago, Chile

[10] Department of Physics, Florida State University, Tallahassee, FL 32306, USA

[11] School of Physics, O'Brien Centre for Science North, University College Dublin, Belfield, Dublin 4, Ireland

[12] Departamento de Física Teórica y del Cosmos, Universidad de Granada, 18071 Granada, Spain

[13] Department of Particle Physics and Astrophysics, Weizmann Institute of Science, Rehovot 76100, Israel

[14] Astronomical Observatory, University of Warsaw, Al. Ujazdowskie 4, 00-478 Warszawa, Poland

[15] Department of Physics and Astronomy, University of Southampton, Southampton SO17 1BJ, UK

[16] Astrophysics Research Institute, Liverpool John Moores University, IC2, Liverpool Science Park, 146 Brownlow Hill, Liverpool L3 5RF, UK

[17] SRON, Netherlands Institute for Space Research, Sorbonnelaan 2, 3584 CA Utrecht, The Netherlands

[18] Department of Astrophysics/IMAPP, Radboud University, PO Box 9010, 6500 GL Nijmegen, The Netherlands

[19] Tuorla Observatory, Department of Physics and Astronomy, University of Turku, 20014 Turku, Finland

[20] DTU Space, National Space Institute, Technical University of Denmark, Elektrovej 327, 2800 Kgs. Lyngby, Denmark

[21] Institute for Astronomy, University of Edinburgh, Royal Observatory, Blackford Hill EH9 3HJ, UK

[22] Birmingham Institute for Gravitational Wave Astronomy and School of Physics and Astronomy, University of Birmingham, Birmingham B15 2TT, UK